

RADBOD UNIVERSITY NIJMEGEN



FACULTY OF SCIENCE

Timing at the ATLAS detector

THE CHALLENGES AND POSSIBILITIES OF TRACK-TIME ASSOCIATION

THESIS MSc. PHYSICS

Author:

Saskia OKKERMAN

Supervisor:

dr. Mengqing WU

Second reader:

dr. Katherine MULREY

Abstract

In the coming years the Large Hadron Collider (LHC) will be upgraded to run at an instantaneous luminosity of $5 \times 10^{34} \text{ cm}^{-2}\text{s}^{-1}$ compared to current Run 3's $2 \times 10^{34} \text{ cm}^{-2}\text{s}^{-1}$. In order to adapt to this change the ATLAS detector will undergo a number of transformations, among which is the addition of a timing detector in the forward region. The High Granularity Timing Detector (HGTD) is still in development, but once installed it will be the first timing detector at ATLAS. The HGTD will provide timing at design resolution of 30 ps before irradiation for tracks in the $2.4 < |\eta| < 4.0$ range. This thesis presents a study of the performance of current methods for assigning tracks time with HGTD hits based on simulated high-transverse momentum muon samples. These methods are based on spatial Inner Tracker (ITk) to HGTD track extrapolation and work well for muons, but for pileup tracks and tracks from secondary particles this extrapolation is significantly less effective. Furthermore, this thesis explores the possibilities of using track-time to improve pileup filtering for muon isolation. It is shown that time-cuts can have significant impact on muon isolation efficiency.

December 27, 2024



Contents

1	Introduction	3
2	The Pileup Problem	4
2.1	The ATLAS Detector	4
2.2	The High-Luminosity Age	5
2.3	Timing as a Solution	6
3	The High Granularity Timing Detector	8
3.1	Disk Design	8
3.2	Low Gain Avalanche Detectors	9
3.2.1	Time Resolution and Sensor Requirements	9
4	Tracking and Reconstruction	12
4.1	The Inner Detector and the Inner Tracker	12
4.2	Track Parameters	13
4.3	Vertex Reconstruction	13
4.4	Muon Reconstruction	14
5	Simulation and Sample Generation	15
5.1	Monte Carlo Production Chain	15
5.2	HGTD Sample Generation	15
5.2.1	ITk to HGTD Extrapolation	16
5.2.2	Single Muon Samples	16
5.2.3	$Z \rightarrow \mu\mu$ Samples	16
5.2.4	Hit Time and Clustering	18
6	Track-Time Association Performance	19
6.1	Track and Muon Selection	19
6.1.1	Base-line Kinetic Track-Cuts	19
6.1.2	Prompt and Stable Particles	19
6.1.3	Truth Muon Matching	20
6.2	Track-Time Association	20
6.2.1	Track-Time Computation	20
6.2.2	Track-Time Resolution	23
6.2.3	Track-Time Matching Quality	23
6.3	Results	25
6.3.1	Muon Selection	25
6.3.2	Track-Time Association Quality	26
6.3.3	Pileup vs Track-Time Efficiency	26
6.3.4	Pileup Track-Time	29
7	Muon Isolation	32
7.1	Isolation Variables	32
7.2	Track Selection	33
7.2.1	Track-to-Vertex Association	33
7.3	Adding Timing	33
7.4	Muon Selection	34
7.5	Results	34
7.5.1	Track-Time Quality	34
7.5.2	Nominal Time-Cut	36
7.5.3	Isolation Efficiency	36
7.5.4	Track-To-Vertex-Association	37
8	Conclusion and Outlook	39
8.0.1	Outlook	39

9	Appendix	41
9.1	Code	41
9.2	Track Reconstruction	41
9.3	Muon Reconstruction Continued	41

1 Introduction

Fundamental high-energy physics is a field of endless questions, questions that have been a driving force behind some of history's most influential technological discoveries and developments. To this day, the desire to gain an ever deeper understanding of our universe inspires endless efforts towards innovation. A prime example is the development of a timing detector at CERN's ATLAS experiment, the High Granularity Timing Detector (HGTD). Up until now, particle detection at ATLAS has relied solely on spatial measurements and the addition of timing is predicted to significantly improve the detector's capabilities for future research. It is one of many planned changes to the ATLAS detector aimed to adapt to the upcoming upgrade of the Large Hadron Collider (LHC). This upgraded version of the LHC, the High-Luminosity LHC, is marked by a significant increase in the instantaneous luminosity in the accelerator; from $2 \times 10^{34} \text{ cm}^{-2}\text{s}^{-1}$ to $5 \times 10^{34} \text{ cm}^{-2}\text{s}^{-1}$. [1] The consequent increase in particles produced in the collisions of the HL-LHC complicated data-taking. The addition of timing to the ATLAS experiment is one of the proposed solutions to maintain current data-taking performance, but its development is complicated by many factors such as spatial limitations, material and technical requirements. The development of the HGTD must be in accordance with all these factors.

This thesis focuses specifically on the performance of the currently available HGTD simulation and track-time association methods for high- p_T muons with updated Inner Tracker geometry and explores the possible benefits of timing information in the context of muon isolation computation. First, the motivation behind the development of a timing detector is given as well as an overview of the current HGTD design and its technical requirements. Sections 4 and 5 introduce important concepts in detection and reconstruction at ATLAS, as well as the samples used in this thesis and the methods used to produce them. Once this necessary background is established, the two main questions that concern this thesis are explored. These being how to best match timing measurements to particle's passing through the detector and how to use this information to improve physics reconstruction. In Section 6, the tools and selection working points (WP) used to study track-time association are described and studied to establish the effectiveness of these methods for muon samples. Subsequently, Section 7 details the methods used to study muon isolation using time information and the corresponding results.

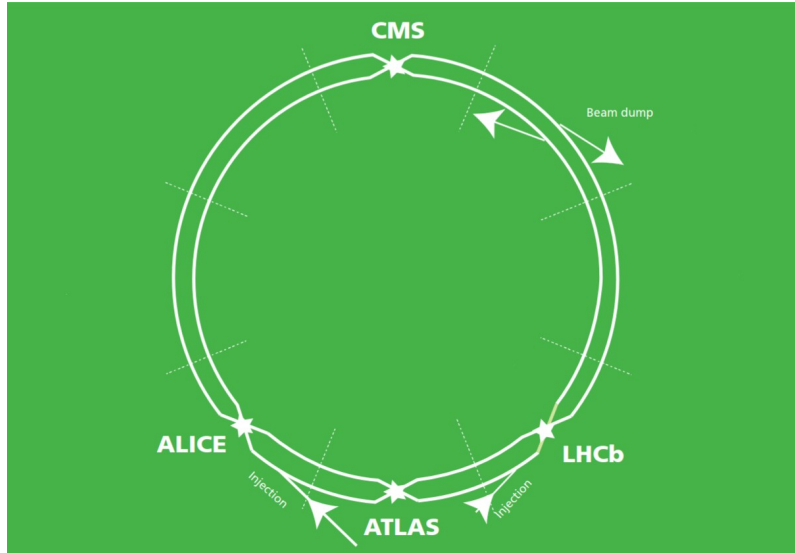


Figure 1: Schematic overview of the LHC layout and its four main detectors. Figure taken and edited from [2].

2 The Pileup Problem

The Large Hadron Collider (LHC) is the world’s largest and most powerful particle accelerator. Working in tandem with the ATLAS detector, it has played a vital role in fundamental physics research since it first achieved collisions in 2010, such as with the discovery of the Higgs boson in 2012 and by enabling continued high-precision probing of electroweak scale physics. The current iteration of the LHC (Run 3) is able to produce proton-proton collisions at $\sqrt{s} = 13.6$ TeV centre-of-mass energy and consistently runs with an instantaneous luminosity of $2 \times 10^{34} \text{ cm}^{-2}\text{s}^{-1}$, twice its original design luminosity.[1] The LHC is able to reach such high collision energies by magnetically accelerating two beams of proton clouds, *bunches*, in opposite directions through a circular 27 km long beam-pipe and letting them cross at four collision points where detectors are stationed (see Figure 1 for an overview). The bunches in the LHC beams contain approximately 1.1×10^{11} protons each and cross around every 25 ns.[2] Some fifty, primarily soft scatter, proton-proton collisions occur during each bunch-crossing. The positions of these collisions in the detector are referred to as *primary vertices*. Typically only one per bunch-crossing is of interest; the hard-scatter vertex. This is an elastic collision typically with high transverse momentum p_T , often of a specific production process. It is essential for the quality of physics research done with ATLAS data, that this collision and its products can be correctly identified and reconstructed. However, bunch-crossings mostly produce inelastic, soft scattering collisions, so-called *pileup collisions*, that greatly complicate measurement. The ATLAS detector is therefore specifically designed to work under these conditions.[3]

2.1 The ATLAS Detector

The ATLAS detector at CERN is one of the world’s most advanced high energy particle detectors, designed to capture the traces of particles produced in collisions in the LHC. It is a general purpose detector, meaning it is not specialised to detect any specific type of particle. Instead, it consists of numerous sub-detectors each designed to measure different particle characteristics. Figure 3 shows a schematic overview of the ATLAS detector.[1]

ATLAS uses a right-handed coordinate system centred around the nominal interaction point (IP), the geometrical centre of the detector. The x -axis points towards the centre of the LHC ring and the y -axis points upwards. The z -axis runs parallel to the beam-pipe at the IP. The detector is approximately symmetric along the ϕ -axis and variables are often studied as functions of the pseudo-rapidity. This is a quantity denoted by η and defined as [3]:

$$\eta = -\ln \tan \frac{\theta}{2}.$$

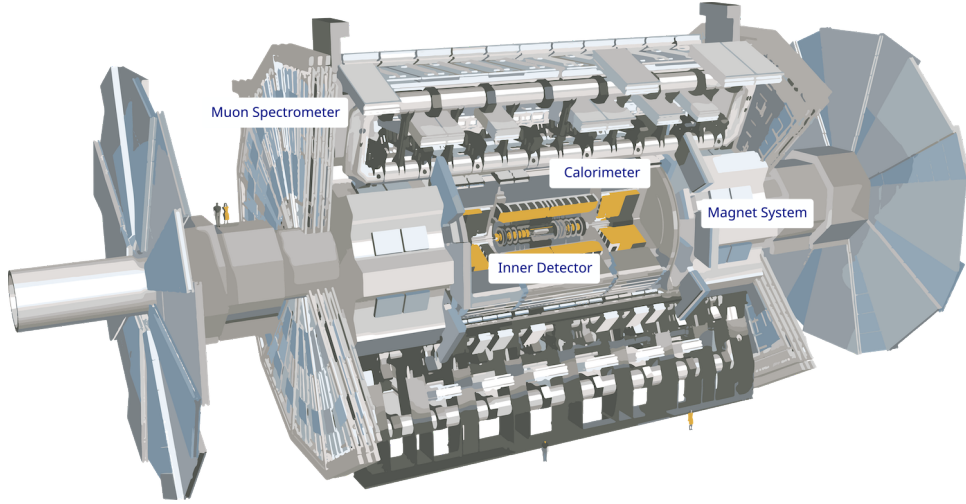


Figure 3: Schematic of the ATLAS detector, labelled for some of its main components. Taken from [5], the labels were added for this thesis.

For the sake of perspective, Figure 2 illustrates the behaviour of η in the $r - z$ plane.

The detector is designed in such a way that it covers nearly the full 360° around the IP. It is comprised of several sub-detectors with a cylindrical section concentric around the beam pipe, the *barrel*, and a section perpendicular to the beam on either side of the bunch-crossing, the *end-caps*. Figure 4 gives a sectional view of the ATLAS detector and illustrates how the traces left by particles traversing ATLAS differ depending on particle type. Particles produced at the IP first travel through the Inner Detector (ID), which tracks the trajectories of charged particles. This is one of the most important (existing) sub-detectors at ATLAS in the context of this thesis and its workings are detailed in Section 4. The Inner Detector is surrounded by an electromagnetic calorimeter, a hadronic calorimeter and a muon spectrometer. The calorimeters provide measurement of positions and energies of charged and neutral, electromagnetically or strongly interacting particles. The muon spectrometer (MS) is another tracker primarily used for muon tracking and identification. All these sub-detectors combined are used to recognise particle types, filter out pileup and reconstruct the physics processes that occurred at the IP.[1]

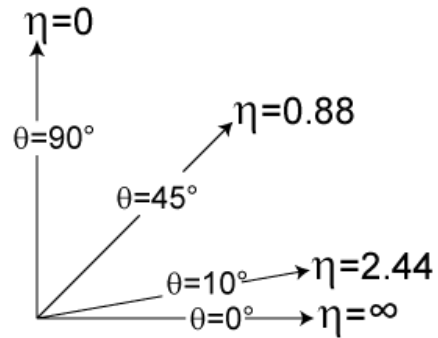


Figure 2: Illustration of the behaviour of pseudorapidity compared to θ . [4] Within ATLAS, the horizontal axis is the z -axis along the beam pipe and the vertical axis is the r -axis.

2.2 The High-Luminosity Age

As mentioned, for the upcoming upgrade to the LHC known as the High Luminosity Large Hadron Collider (HL-LHC) and scheduled to start operation in 2030, the instantaneous luminosity will become $5 \times 10^{34} \text{ cm}^{-2}\text{s}^{-1}$ compared to $2 \times 10^{34} \text{ cm}^{-2}\text{s}^{-1}$ of the current LHC run. The aim of this update is to increase the accelerator's yield to an integrated luminosity of 350 fb^{-1} per year. Higher yield increases the likelihood of measuring low-cross-section processes, however, it also causes an increase of pileup collisions per bunch-crossing and forces dramatic changes to the ATLAS detector.[7]

Instead of the current Run 3 pileup rate of around $\langle \mu \rangle = 50$, the HL-LHC will see pileup of approximately $\langle \mu \rangle = 200$. This pileup increase translates to a jump in local vertex density (see Figure 5a), which the

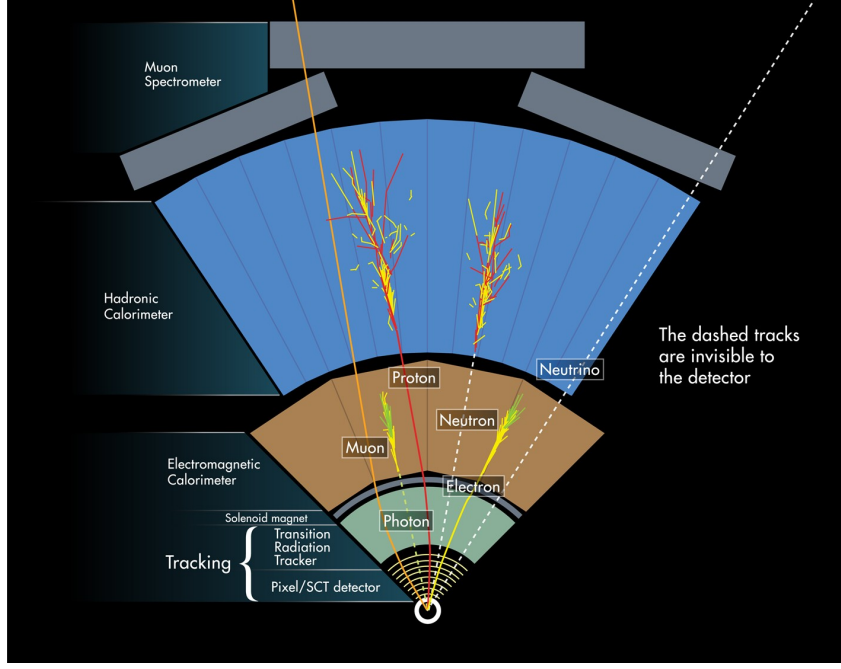
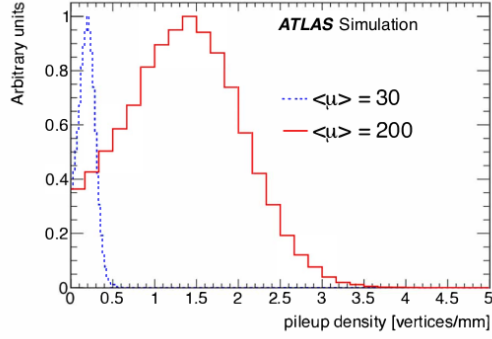


Figure 4: Schematic illustration of a slice of the ATLAS detector, perpendicular to the beam pipe, including the various sub-detectors and a number of characteristic particle tracks.[6]

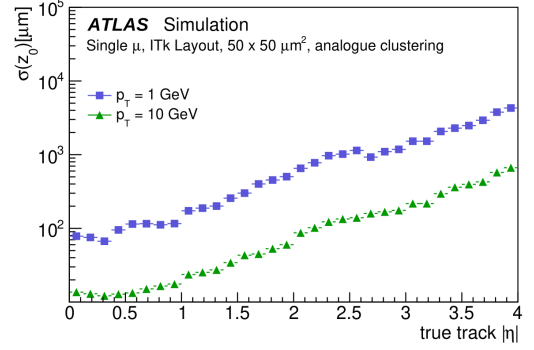
current ATLAS detector is not equipped to handle, neither in terms of resolution capabilities nor material requirements such as radiation hardness. Figure 6 illustrates what such a high pileup bunch-crossing would look like inside ATLAS compared to a $\langle\mu\rangle = 50$ bunch-crossing. It shows that the density of charged particles passing through the detector is especially high parallel to the beam-pipe, along the z -axis. This is called the *forward* region. These particles typically have low transverse momentum resulting from soft-scatter pileup collisions and result in a rapid decrease in detector resolution along the z -axis as a function of η . This is one of the primary motivations behind ongoing efforts to improve and upgrade the ATLAS’s existing sub-detectors. The ID will notably be exchanged for a new, all-silicon Inner Tracker (ITk). This detector will expand the tracking reach of the ID from $|\eta| < 2.5$ to $|\eta| < 4$ and improve spatial resolution.[3] The ITk is discussed in more detail in Section 4.1. If the spatial resolution is better than the average distance between two vertices, individual pp -collisions can be separated. The simulated $\langle\mu\rangle = 200$ bunch-crossing in 5a has a average local vertex density of 1.44 vertices/mm. Figure 5b shows that with the ITk, the detection error in z is sufficient in the low- $|\eta|$ range, but exceeds the inverse of this value in the high- $|\eta|$ region. The addition of the ITk will, therefore, not be enough on its own to compensate for the extreme conditions at the HL-LHC.[3]

2.3 Timing as a Solution

The current ATLAS detector relies solely on spatial measurements to reconstruct the physics processes that occur as a result of high-energy, beam collisions. The collisions in an HL-LHC beam-crossing are expected to be spread in time with a width of 175 – 260 ps and have a Gaussian spread along the beam-pipe between 30 and 60 mm (see Figure 7). High resolution timing information could, therefore, be used to help distinguish between individual vertices when the detector’s resolution in z decays as in Figure 5b. Current strategy is to add a timing detector, the HGTD, only in the high-pseudo-rapidity region.[3] This detector, its design and its performance are detailed in Sections 3 and 5. The timing measurements will be integrated into the pre-existing detector and supplement current and future detection methods.[3]

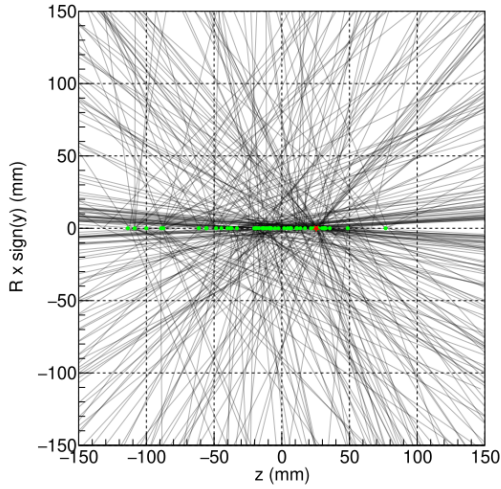


(a)

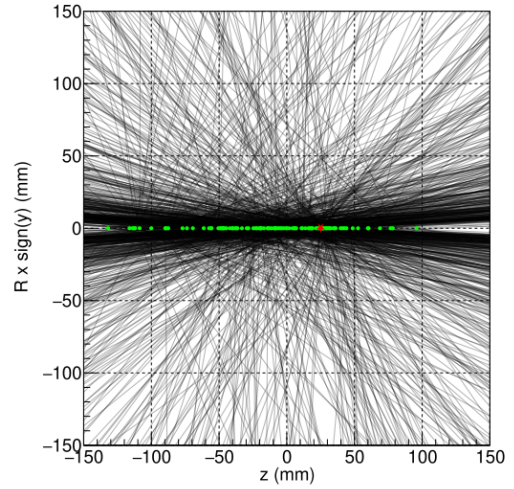


(b)

Figure 5: (a) Local vertex density at generator level for two different degrees of pileup; $\langle\mu\rangle = 30$ and $\langle\mu\rangle = 200$. [3] (b) Resolution of z_0 for single muon samples without pileup as a function of η , comparing 1GeV and 10GeV samples. [3]



(a) Schematic of bunch-crossing with 50 pp -collisions.



(b) Schematic of bunch-crossing with 200 pp -collisions.

Figure 6: Longitudinal view of a (a) $\langle\mu\rangle = 50$ and (b) $\langle\mu\rangle = 200$ bunch-crossing generated from a $t\bar{t}$ sample with $\langle\mu\rangle = 200$. The green dots represent pileup interactions and the red star represents the hard-scatter vertex, chosen as the event's highest p_T collision.

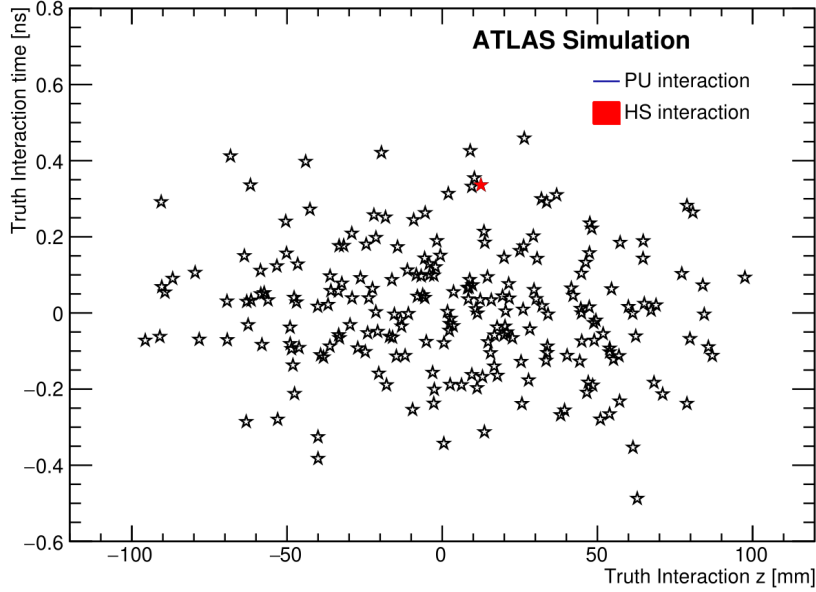


Figure 7: Visualisation of the truth primary vertices in a $\langle\mu\rangle = 200$ bunch-crossing spread in space and time. Edited from [3].

3 The High Granularity Timing Detector

The addition of timing to the ATLAS detector is a promising solution to improve physics object reconstruction and pileup filtering in a high-luminosity environment. However, implementing time detection poses many new technical challenges, exacerbated by the spatial limitations of the existing detector, financial considerations and material requirements. The ATLAS Collaboration’s answer to these challenges comes in the form of the High Granularity Timing Detector (HGTD) in ATLAS’s forward, high- $|\eta|$ region. The HGTD will provide timing measurements for charged high- $|\eta|$ particles at a design resolution of approximately 30 ps, expected to deteriorate to 50 ps throughout an HL-LHC run. As discussed in Section 2.2, many of the charged particles moving through the detector in the forward region are produced in soft, pileup events. Adding timing information to these particles is expected to significantly improve pileup filtering and physics object reconstruction in this region. Additionally, the HGTD offers the possibility of taking precise online luminosity measurements for individual bunches while the HL-LHC is running, and highly precise integrated luminosity measurements offline. These added functionalities of the HGTD will lead to reduced systematic uncertainties and improved detector performance overall.[3] In July of 2020, a technical design report (TDR [3]) was published summarising the developments within the different groups working on HGTD design and implementation. Much of the HGTD as it is described in this thesis is in accordance with this document barring updates to geometry that have been implemented since.

3.1 Disk Design

The HGTD will consist of two ring-shaped detector units placed at approximately $z = \pm 3500$ mm on either side of the IP. It will be fit in the gap between the ITk and end-cap calorimeters (see Figure 8), perpendicular to the beam pipe. Both HGTD units consist of two disks; cooling plates with sensors and sensor electronics attached to either side. This way the HGTD will have four sensor layers on either side of the IP and a charged particle passing through an HGTD unit can leave up to four energy deposits or *hits*.

The disks of the HGTD will span an area from $r = 100$ mm to $r = 1000$ mm, but the detector’s active area will only cover range $120 \text{ mm} < r < 660 \text{ mm}$, or $2.4 < |\eta| < 4.0$. The remaining outer area will hold peripheral electronics. The disks are covered with 20×40 cm sensor modules containing $1.3 \text{ mm} \times 1.3 \text{ mm}$ pixels (see Section 3.2). The sensor layers on either side of the cooling disks are placed at a relative angle of 15° to 20° (see Figure 9) to optimise sensor overlap. The active area is made up of three rings with varying degrees of sensor overlap. In the inner ring, closest to the beam-pipe in range $120 \text{ mm} < r < 230 \text{ mm}$, the sensors of two active layers overlap on approximately 70% of the disk’s

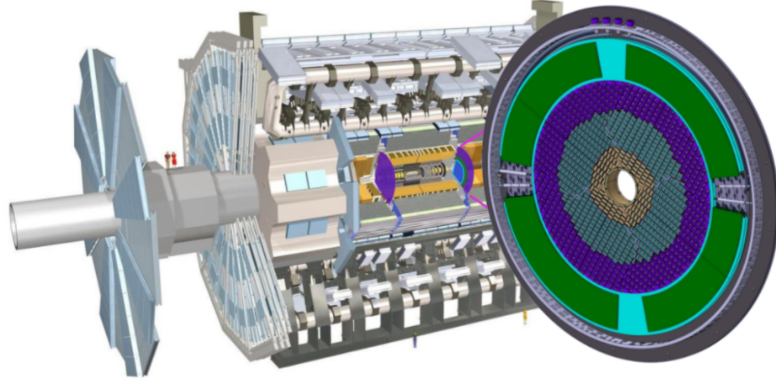


Figure 8: The placement of the HGTD disks in the Atlas detector.[3]

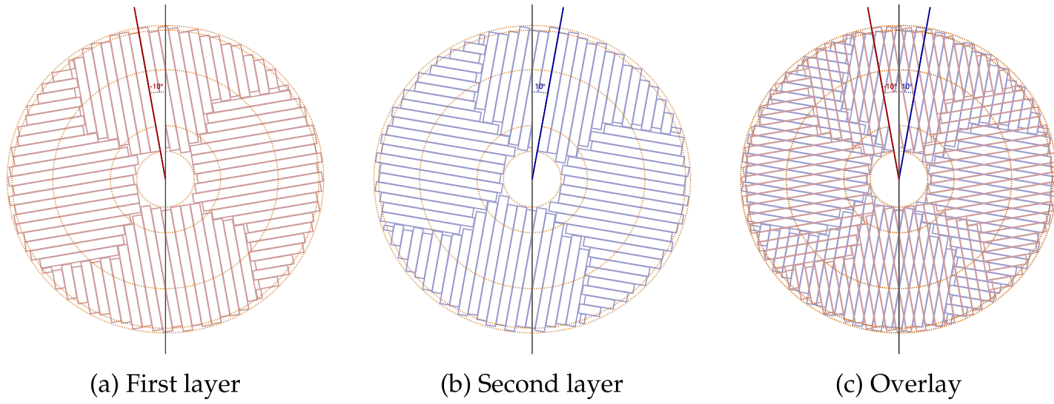


Figure 9: Schematic of two HGTD sensor layers and their overlay at a relative angle of 20° . [3]

surface. The middle layer has a sensor overlap of approximately 50% and ranges from $r = 230$ mm to $r = 470$ mm. The outer layer covers the area between $r = 470$ mm and $r = 660$ mm and has around 20% sensor overlap (see Figure 10). This choice was made to approximate consistent performance as a function of r . The mean hit multiplicity i.e. the mean number of hits left in the detector by a particle, varies between the detector rings (see Figure 11).[3]

3.2 Low Gain Avalanche Detectors

The sensors that will be used in the HGTD to provide timing measurements are called Low Gain Avalanche Detectors (LGAD), chosen for their radiation hardness and adaptability. They are n-on-p silicon detectors with an internal gain. They contain a highly-doped p-layer (the avalanche region in Figure 12). When a charged particle passes through an LGAD pad, it generates a current in the silicon by causing a drift of electrons and holes. Once the electrons reach the highly-doped avalanche region, the signal is amplified which makes it possible to achieve high resolution timing measurements. This amplification is called the gain. The read-out electronics register the leading edge of this signal, the *Time of Arrival* (TOA). This depends on when the signal exceeds an amplitude-dependent threshold. As shown in Figure 12b, the signal amplitude generated in the LGADs decreases after irradiation and the slope of the current flattens, which translates to a decay of the sensor's time resolution. In the HGTD, LGAD pads, or *pixels*, of $1.3 \text{ mm} \times 1.3 \text{ mm}$ and with an active thickness of $50 \text{ }\mu\text{m}$ will be used.[3]

3.2.1 Time Resolution and Sensor Requirements

To reach the resiged 30 to 50 ps track-time resolution in the HGTD when combining multiple hits, the LGAD sensors must be able to reach a resolution of 35 ps before irradiation and this performance must

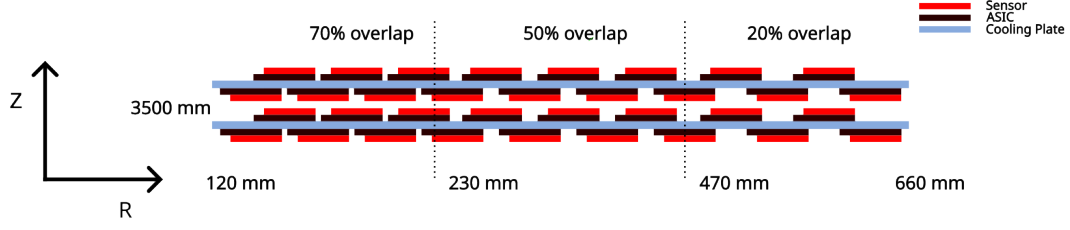


Figure 10: Schematic of an HGTD unit illustrating the sensor layers with different degrees of overlap.

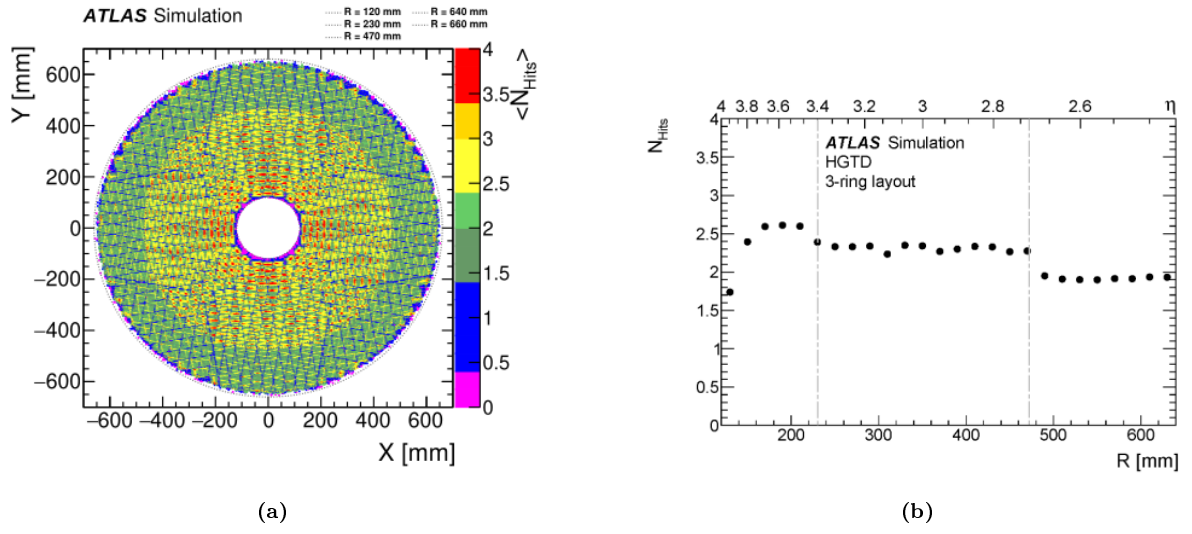


Figure 11: Mean hit multiplicity in the HGTD as a function of (a) x and y and (b) r . In (b) the grey dashed lines indicate the three ring design. These figures were generated with simplified HGTD simulations.[3]

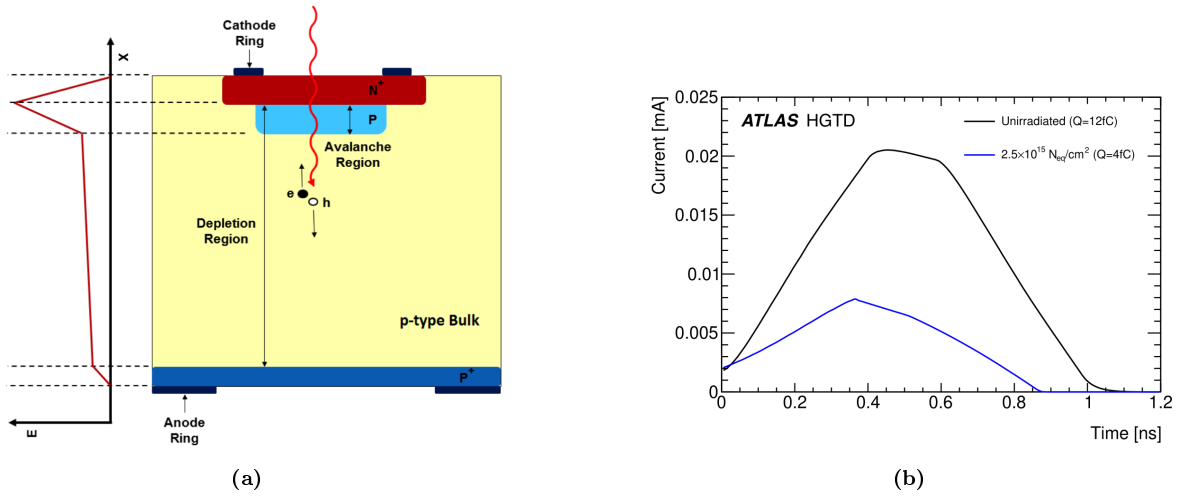


Figure 12: Schematic cross section of an LGAD (a) and a simulated current in an LGAD in time before and after irradiation (b).[3]

not decay to worse than 70 ps after 4000fb^{-1} irradiation.

The hit-time resolution has three main contributions;

$$\sigma_{\text{tot}}^2 = \sigma_{\text{L}}^2 + \sigma_{\text{el}}^2 + \sigma_{\text{clock}}^2. \quad (1)$$

σ_{L} is the uncertainty caused by Landau fluctuations, which refers to fluctuations in TOA caused by non-uniform charge deposits along the particle path in the sensor. This contribution is reduced for thinner sensors. For the 50 μm LGAD pixels that will be used in the HGTD, this contribution is approximately 25 ps. σ_{el} is the readout electronics' contribution (jitter and time-walk) expected to be around 25 ps as well. Lastly, σ_{clock} refers to the clock jitter uncertainties which will contribute some 15 ps. The digitisation error can be made negligible.[3]

In order to provide bunch-by-bunch luminosity measurements, the pads should be able to distinguish between hits in the same pad from consecutive bunch-crossings and provide the sum of hits per module for each bunch-crossing.[3]

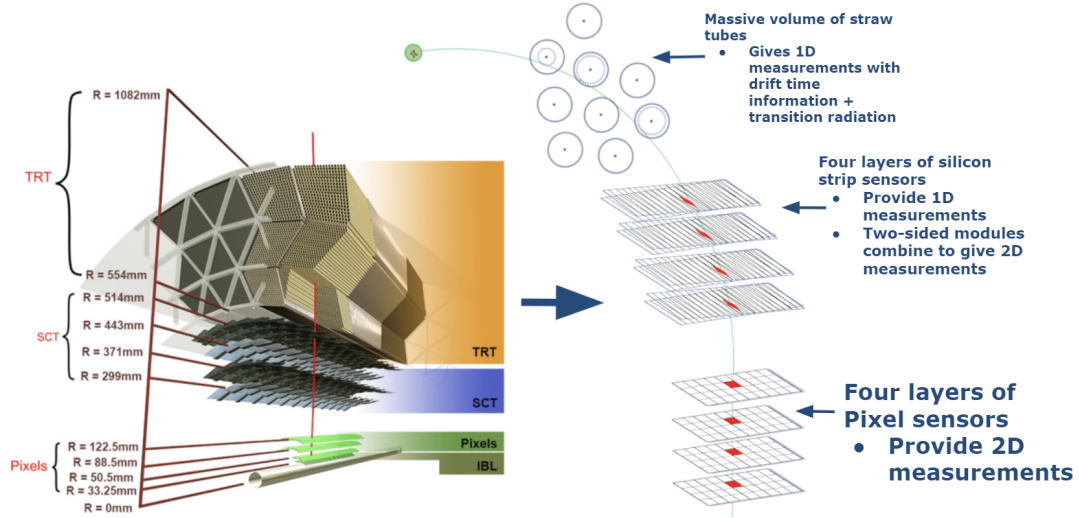


Figure 13: Simplified radial overview of the Run 3 Inner Detector as well as a schematic particle trajectory.[8]

4 Tracking and Reconstruction

The HGTD will work in tandem with the existing ATLAS detector and the ITk. Assessing its performance should therefore be done in the context of pre-existing detection and reconstruction methods. Especially relevant to this thesis are tracking and muon reconstruction.

4.1 The Inner Detector and the Inner Tracker

Tracking in the context of the ATLAS detector refers to the process of detecting and reconstructing the trajectories of charged particles by identifying sets of energy deposits, *hits*, left in the detector by the same particle. It is an essential functionality of the ATLAS detector and plays a crucial role in vertex reconstruction and particle identification.

As mentioned previously, tracking at ATLAS is currently done by the Inner Detector (ID). The ID is designed to track charged particles moving through the detector in range $|\eta| < 2.5$. Figure 13 shows a radial view of its layout. It consists of three sub-detectors, the innermost of which is the high-granularity silicon Pixel detector, with four concentric barrel layers and three disks at each end-cap. The Pixel detector is surrounded by the Semiconductor Tracker (SCT) and the Transition Radiation Tracker (TRT). The SCT has four barrel layers of silicon strip sensors and nine end-cap disks on either side. The outer layer of the ID, the TRT, is filled with straw tubes that provide one-dimensional measurements including drift-time information.[8]

To adapt to the HL-LHC's increase in pileup and maintain tracking performance, the ID will be fully replaced by the all-silicon ITk. The ITk will have high sensor granularity to provide high-resolution tracking, extend the tracking reach of the ID to the high pseudo-rapidity region and be made of highly radiation-hard material, in order for it to endure the high degrees of radiation that will be present near the IP during the high luminosity run. Figure 14 is a schematic representation of recent ITk design (ITk layout *03-00-00*). The ITk will consist of two sub-detectors; a Pixel detector nearest to the beam pipe, similarly to in the ID, and a Strip detector. The Strip detector is made up of four double sided detector strips in the barrel region and six disks at either end-cap. This covers the tracking in $|\eta| < 2.7$. The Pixel sub-detector has five barrel layers parallel to the beam pipe and numerous inclined or vertical, thin, ringed end-cap disks that provide tracking in $|\eta| < 4$. [9]

As the ITk is still in development as of the writing of this thesis, it is not yet certain how best to use ITk measurements for track reconstruction while minimising the computational load. Extensive research is being done on novel track reconstruction techniques, such as *GNN4ITk* [10], which uses Graph Neural

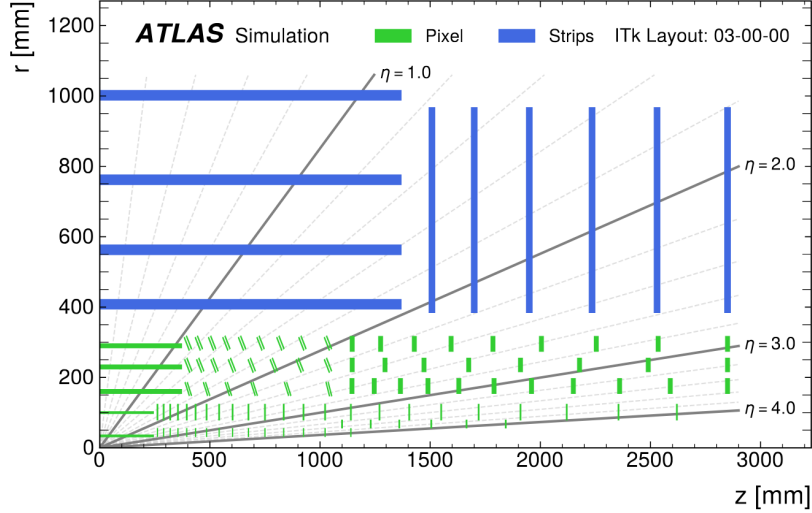


Figure 14: Schematic overview of a quadrant of the most recent 03-00-00 ITk layout.[9]

Networks to optimise seed-finding. Despite the significant change in detector design, the general concept of tracking remains the same and track reconstruction methods used for the ID are also used for simulated ITk data.[9] Section 9.2 in the appendix details some of these specific reconstruction methods.

4.2 Track Parameters

A reconstructed track is defined by the detector hits that were used in the reconstruction and track parameters that describe its trajectory. In ATLAS, a perigee representation with five parameters is used to describe reconstructed tracks, i.e. a track's coordinates are defined in terms of its nearest approach to a point of reference. When computed relative to the mean position of the luminous region of a bunch-crossing, the *beam spot* position, these parameters are referred to as a track's *defining parameters*:

$$\mathbf{q} = (d_0, z_0, \phi, \theta, q/p) \quad (2)$$

Where d_0 and z_0 are the defining transverse and longitudinal impact parameters, respectively. ϕ and θ are simply the track's defining ϕ and θ coordinates and q/p is the corresponding charge over momentum. Figure 15 illustrates how the first four of these parameters are defined. The so-called *defining parameters* of a track refer to the track's point nearest to the beam spot position, but track parameters along a particle trajectory within the detector are typically defined relative to the nearest detector layer. For a reconstructed track, the track parameters at each hit in the detector are registered along side the track fit.[8]

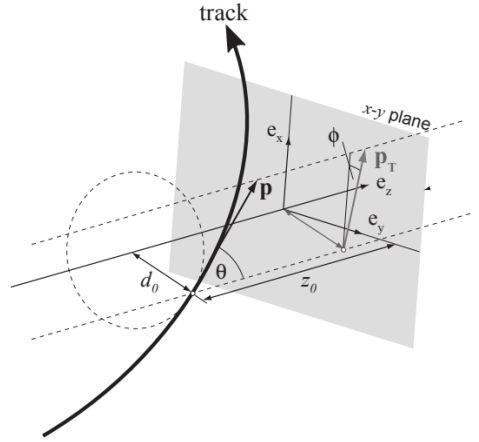


Figure 15: Schematic illustration of track parameters in the perigee representation.[8]

4.3 Vertex Reconstruction

Accurate vertex reconstruction is crucial for the quality of further physics analysis at the ATLAS detector. After track reconstruction, the obtained track candidates are used to find the originating primary vertices using a specialised vertex reconstruction algorithm, the *adaptive multi vertex fitter* (AMVF). Figure 16 gives a schematic overview of this fitting procedure. It starts with a Gaussian Track Density Seed Finder that identifies possible vertices based on the distribution of tracks along the beam axis. Each track is modelled as a Gaussian probability distribution in the $r-z$ plane, centred around the associated (d_0, z_0) coordinate point. The sum of these distributions provides a total density of tracks as a function of z . This distribution is used to iteratively look for the global maximum, which is used as the vertex

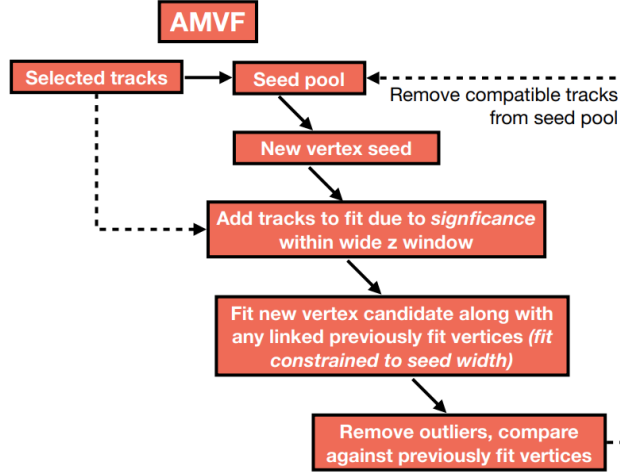


Figure 16: Schematic of the AMVF approach to vertex reconstruction.[12]

seed position. After a vertex fit is attempted on this seed, the tracks matched to it are taken out of the sum of track-density and a new global maximum is identified. This then serves as the next vertex seed. At each vertex fitting, all vertices that were already fit are refit as well. This ultimately results in tracks being matched to multiple vertices, weighted for likelihood.[11]

4.4 Muon Reconstruction

As muons are charged leptons, they leave a track in the Inner Detector much like electrons do. However, muons do not produce a shower in the calorimeter. Instead, they pass through the calorimeter with minimal loss of energy to reach the detector's outer-most layer, the Muon Spectrometer (MS), where they leave another track. Muons can be reconstructed in several ways using different combinations of ID or ITk tracks (referred to here as ID tracks), calorimeter measurements and MS tracks;

- *Combined* muons are reconstructed with a global refit of matched ID and MS tracks.
- *Segment-tagged* muons are made up of an ID track matched to a MS segment without global refit.
- *Calorimeter-tagged* muons consist of an ID track matched to a characteristic calorimeter energy deposit.
- *Stand alone* muons consist only of a MS track extrapolated to the beam-line.

Figure 17 schematically illustrates these different reconstructed muon traces in the ATLAS detector.[13] Appendix Section 9.3 gives a more detailed description of muon reconstruction methods.

The quality of muon reconstruction is defined using sets of selection criteria, *working points* (WP), ranging from "VeryTight", "Tight", "Medium", "Loose" and "VeryLoose". These categories differ depending on the muon reconstruction type and put requirements on variables such as track fit quality, q/p significance and $|\eta|$. Tight working points prioritise reconstruction accuracy over efficiency, while loose WP's are optimised for efficiency. Only the "VeryLoose" category is not a recommended muon selection working point.[14]

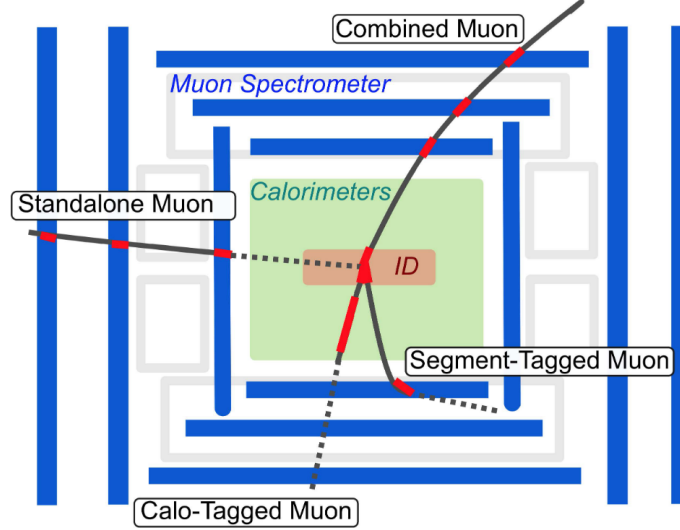


Figure 17: Schematic of different muon reconstruction methods.[13]

5 Simulation and Sample Generation

Almost all possible ATLAS production processes are managed within the Athena software framework; from event generation, to detector output simulation, to physics object reconstruction and more. Athena is also used to process real physics data.[15] However, since both the HGTD as well as the HL-LHC are still in development, this thesis uses simulated data produced from simulated detector geometries. The simulation and analysis was done using Athena 24.

5.1 Monte Carlo Production Chain

Within Athena, numerous tools for specialised physics simulation are available. These tools are used in a Monte Carlo (MC) production chain to produce full detector and physics simulations which can be used to compare theoretical models, test detector performance and improve algorithms.

The MC production chain starts with event generation. This refers to the simulation of high-energy particle collisions and their products as sets of four-momenta. The event generator output models idealised detector performance and is not a realistic representation of detector output. Particle interactions with the detector are then simulated with the use of a geometrical model of the ATLAS detector made with the *GeoModel* toolkit and *Geant4*, a toolkit for simulating particle interactions with matter. Simulated detector hits are put through a digitisation step to emulate detector output. In this step, simulated events of a specifically curated physics process such as $Z \rightarrow \mu\mu$ and VBF $H \rightarrow \text{invisible}$, are often overlaid with pileup.

After digitisation, the output is reconstructed into *physics objects* such as tracks, vertices, muons, electrons, missing transverse energy (MET) and jets. The reconstruction process for simulation is largely identical to real data processing as described in Section 4. However, in the case of simulated data, truth information about the underlying Monte Carlo event generation is recorded and can be used to test simulation performance. Truth information includes truth particles and their kinetic properties, particle links that match particles and tracks to their originating parent particles and associated production vertices, and much more.[16]

5.2 HGTD Sample Generation

The samples used in this thesis to study HGTD performance and track-time association were generated with the *ATLAS-P2-RUN4-03-00-01* geometry, as described in Section 4.1, in Athena Release 24 (Rel. 24). They contain information on simulated HGTD hits and reconstructed high- p_T muons.

Sample Type	p_T [GeV]	$\langle\mu\rangle$	Sample ID
Single μ	100	0	mc21_14TeV.902028.PG_single_muon_Pt100_etaFlatnp23_4l.recon.AOD. e8481_s4272_r15365_tid40114733_00
Single μ	100	60	mc21_14TeV.902028.PG_single_muon_Pt100_etaFlatnp23_4l.recon.AOD. e8481_s4272_r15366_tid38028695_00
Single μ	100	140	mc21_14TeV.902028.PG_single_muon_Pt100_etaFlatnp23_4l.recon.AOD. e8481_s4272_r15367_tid38028700_00
Single μ	100	200	mc21_14TeV.902028.PG_single_muon_Pt100_etaFlatnp23_4l.recon.AOD. e8481_s4272_r15368_tid37963419_00
$Z \rightarrow \mu\mu$	100	0	mc21_14TeV.601190.PhPy8EG_AZNLO_Zmumu.recon.AOD. e8481_s4272_r15365_tid37891244_00
$Z \rightarrow \mu\mu$	100	200	mc21_14TeV.601190.PhPy8EG_AZNLO_Zmumu.recon.AOD. e8481_s4272_r16070_tid41716293_00

Table 1: Overview of all the Monte Carlo samples used in this study

5.2.1 ITk to HGTD Extrapolation

In current Run 4 sample generation, ITk tracks are reconstructed separately from the HGTD hits. Associating the ITk tracks to HGTD hits is done using an iterative path extrapolation procedure. First, the last measurement of a track in the ITk is taken as the starting point. The track is then extended to the HGTD surfaces using a progressive Kalman filter. In each HGTD sensor layer, the presence of clusters or hits near a given ITk track is evaluated. The spatial compatibility is tested by extending the track to each nearby cluster in a forward filtering step. From the spatially compatible clusters, the one with the lowest χ^2 value is chosen. The extrapolation is only successful if it passes a $\chi^2/n.d.f. < 5$ requirement. This then becomes the new starting point of the extrapolation and the process is repeated. Figure 18 illustrates this process schematically. As a result of this extrapolation process, samples generated this way contain a link between ITk tracks and HGTD hits and truth information is stored on both these types of objects. The ITk to HGTD extrapolation uses only spatial information to match HGTD hits to tracks.[3]

5.2.2 Single Muon Samples

Most of the samples used in this thesis were generated using the *Geant4* particle gun method (labelled as "Single μ " in Table 1). This method simulates single primary particles of a given type and momentum and generates a corresponding primary vertex.[17] The particle gun samples used in this thesis consist of single muon particle gun simulations at $p_T = 100$ GeV with an overlay of pileup tracks. Four different degrees of pileup were studied: $\langle\mu\rangle = 0$, $\langle\mu\rangle = 60$, $\langle\mu\rangle = 140$ and $\langle\mu\rangle = 200$. These samples do not contain full truth records of the pileup, i.e. the truth particles that produced the pileup tracks and corresponding primary vertices were not saved after simulation.

5.2.3 $Z \rightarrow \mu\mu$ Samples

In addition to the particle gun samples, two $Z \rightarrow \mu\mu$ samples of $p_T = 100$ GeV were studied; one without pileup and one with $\langle\mu\rangle = 200$. These simulated physics samples were generated with *Pythia 8* and *EvtGen* and therefore include simulations of hadronic decays.[16] The $\langle\mu\rangle = 200$ sample contains full pileup truth.

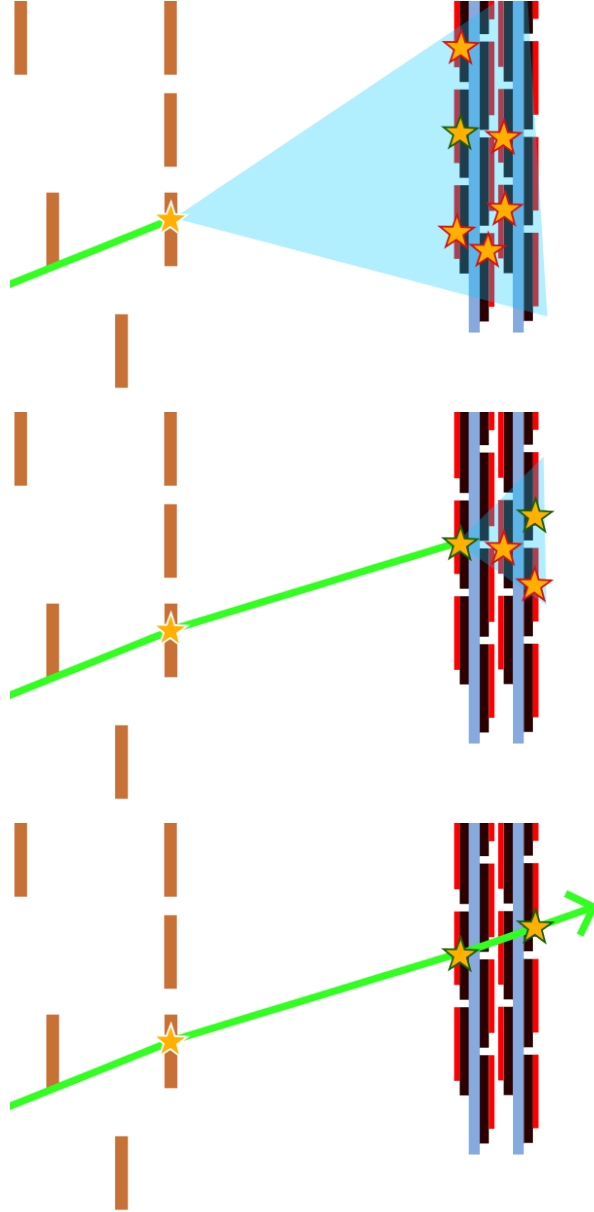


Figure 18: Schematic illustration of the iterative extrapolation of ITk tracks to the HGTD. The green stars represent the best spatial fit chosen over the red hits to be the extrapolation's next starting point.

5.2.4 Hit Time and Clustering

In the ITk-to-HGTD extrapolation procedure, no clustering is applied to the HGTD pads; the timed hits that ITk tracks are matched to are single pixel detector hits. In an early study conducted for the TDR [3], the clustering approaches used showed significant increase in cluster size (see Figure 19). In order to minimise the risk of merging different contributions into a single cluster and consequently contaminating good quality pixel measurements, it was decided to continue without any clustering.

The simulated hit times saved in the samples of Table 1 are the time of arrival with a straight-line time-of-flight correction, i.e.

$$t_{\text{hit}} = TOA - TOF \quad (3)$$

The time of arrival is determined from simulated LGAD read-out as described in 3.2. The time-of-flight correction is computed after a hit has been matched to a track as the time a particle travelling at the speed of light would take to pass from the origin of the track, $(0, 0, z_0)$, to the centre of the relevant HGTD pixel in a straight line. This correction is applied to be able to compare track-times computed with these hit-times to truth vertex times. Hit-time resolution is currently hard-coded to 35 ps.[3]

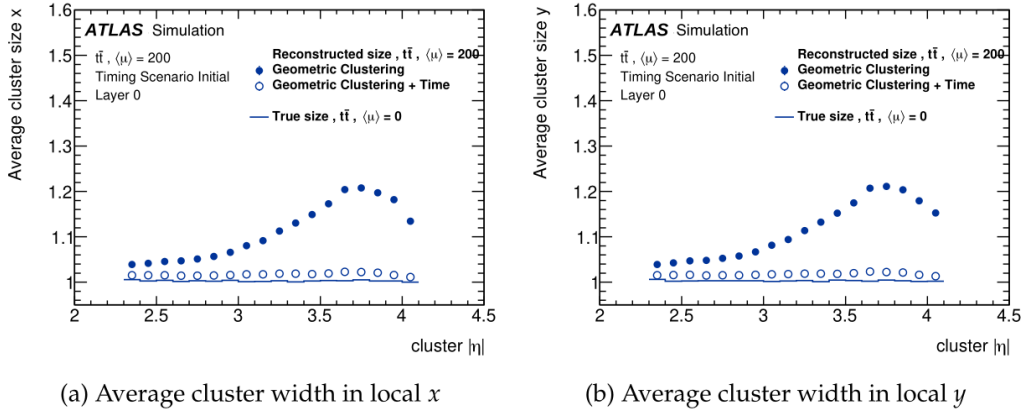


Figure 19: Plots comparing cluster size as a function of $|\eta|$ for three different clustering approaches; geometric clustering only, temporal and geometric clustering, and no clustering.[3]

proton-proton collisions and secondary particles are produced in material interactions. The asymmetrical tail of the secondary particle timing distribution is caused by low- p_T particles and/or particles with a longer path than the straight-line approximation. More realistic physics samples typically also contain simulations of hadronic decays which also produce secondary particles. For physics analyses, only particles that are *prompt* (originating from proton-proton collisions) and *stable* (without decays within the detector) are desired.[3] For track-time association performance studies, secondary particles are filtered out using truth information. This selection requires a track to be matched to a truth particle that is linked to a production vertex. The location of this vertex must fall within $0 < r < 10$ mm and $0 < |z| < 100$ mm, near the IP. The tracks are also checked for decay vertex links; if a particle has undergone some secondary decay before reaching the HGTD, i.e. in range $|z| < 3479$ mm, it is dismissed.

6.1.3 Truth Muon Matching

As described in Section 5.2.2, the samples used in this thesis have different degrees of pileup. When assessing the effects of the HGTD hits left by pileup tracks on the track-time association of muon tracks, the pileup tracks themselves need to be filtered out. To minimise additional uncertainties from muon reconstruction, the choice was made to use only truth muons by requiring tracks to be truth matched to a muon.

6.2 Track-Time Association

Once a given track selection is applied to the data, the track-matched HGTD hits are used to compute track-time. Preliminary track-timing studies done for the HGTD compare two approaches for track-time association; one applies a time consistency check to the HGTD hits associated to a track, while the other does not. In the following, both approaches are summarised along with a method for quantifying quality of track-time association.

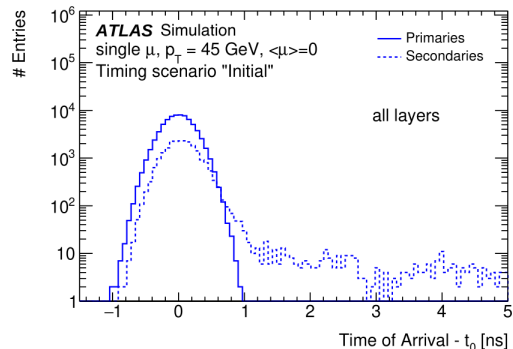


Figure 21: Time distribution of simulated energy deposits in the HGTD, distinguishing primary and secondary particles, for a single muon sample without pileup.[3]

6.2.1 Track-Time Computation

Without applying a time consistency check to a track's associated HGTD hits track-time is computed as the mean of hit-times t_i ;

$$t_{\text{mean}} = \frac{1}{N_{\text{hits}}} \sum_{i=1}^{N_{\text{hits}}} t_i. \quad (4)$$

N_{hits} is the number of hits matched to a track. Where Since the extrapolation algorithm described in Section 5.2.1 is based solely on spatial information, the hits associated to a track may not be consistent in time. Therefore, a cleaning procedure is used to filter out temporal outliers and improve the quality of track-time association. What this procedure entails differs depending on the number of HGTD hits associated to an ITk track after extrapolation.

- **1 hit** In this case the track-time association is passed automatically and the HGTD hit's time becomes the track-time, unless the track falls in range $3.5 < |\eta| < 3.9$. Such a track is required to have at least two hits in order for it to pass. This choice is justified by the high degree of sensor overlap in this region (70%), as well as the large number of HGTD hits left by pileup tracks at high- $|\eta|$. [3]
- **2 hits** The hits are checked for time compatibility:

$$|t_i - t_j| < \Delta t \times \sqrt{\sigma_{t_i}^2 + \sigma_{t_j}^2} \quad (5)$$

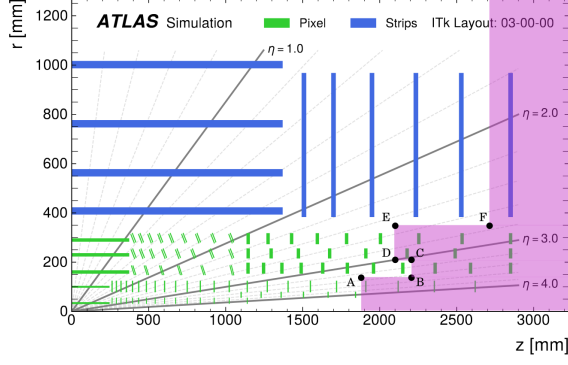


Figure 22: Schematic of ITk layout 03-00-00 with the coloured region in which tracks' last ITk hits are allowed to be in the time consistency check. Figure edited from [9]. The HGTD will be stationed at $z = 3500$ mm. See Table 2 for the exact coordinates.

Point	z [mm]	r [mm]
A	1890	140
B	2200	140
C	2200	205
D	2100	205
E	2100	350
F	2700	350

Table 2: The coordinates in the $r - z$ plane that denote the edges of the accepted region for a track's last ITk hit to be in.

Where t_i and t_j are the individual hit times and σ_{t_i} and σ_{t_j} are the corresponding hit resolutions, set for valid hits to 35 ps. Δt_{cut} is set to 2.

- **3-4 hits** When a track has more than two hits associated to it, the HGTD hit-times must pass a χ^2 cut. The χ^2 value of the hit-times is computed as

$$\chi^2 = \sum_{i=1}^{N_{\text{hits}}} \frac{(t_i - t_{\text{mean}})^2}{\sigma_{t_i}^2} \quad (6)$$

Where t_{mean} is the mean time of all hits as defined in equation 4 and σ_{t_i} is once again the time resolution for each hit. If this does not obey

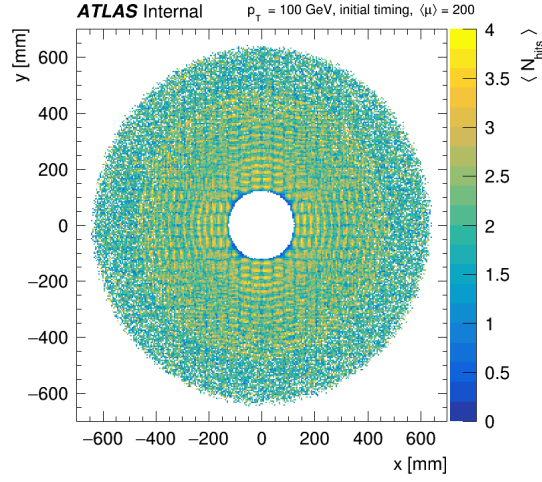
$$\chi^2 < 1.5, \quad (7)$$

the tool iteratively removes one of the hits, recomputes the χ^2 value for each iteration and chooses the hit combination with the lowest χ^2 value. In other words, any hit that is temporally inconsistent with the rest of the hits is filtered out. If this still does not fall under the threshold and more than two hits are left, the process is repeated. If only two hits are left, the requirement of equation 5 is once again imposed. If the hits still do not pass, **no time is assigned to the track**.

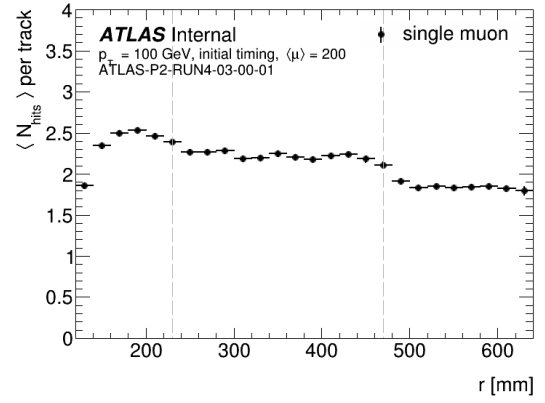
As mentioned, when a track is only matched to a single HGTD hit, the corresponding hit-time becomes the track-time. In the event that more than one hit are left matched to the track after the time consistency check, the track-time is computed as Equation 4; the mean time of the remaining hits. N_{hits} changes as hits get filtered out.

In the time consistency check, an additional track selection is applied to filter out ITk tracks that were not extrapolated from a point near the HGTD. This is done by requiring a track's last hit measurement in the ITk to fall in a space near the HGTD, illustrated in Figure 22. This selection aims to improve overall ITk-to-HGTD extrapolation quality by limiting the distance over which to extrapolate.[3] The cuts used are dependent on ITk design. Table 2 summarises the exact cuts used in this thesis.

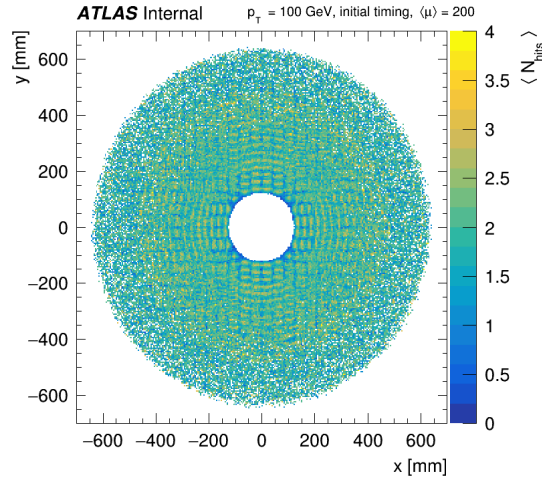
The time consistency check has been designed to improve overall track-time matching by filtering out mismatched HGTD hits and to smooth out track-time resolution as a function of r . As described in Section 3.1, the expected mean hit multiplicity of the HGTD detector differs between the three sensor rings, both due to the varying degrees of sensor overlap and the uneven spread of pileup tracks passing through the detector. Figure 23 shows the impact of the track-time consistency check on mean hit multiplicity as a function of $|\eta|$ for a $\langle \mu \rangle = 200$ single muon sample. The time consistency check lowers hit multiplicity by filtering out outlier hits, which results in a more consistent performance over the three detector rings. Both with and without time consistency check the hit multiplicity in the most inner part of the detector disk is very low. This is due a low rate of sensor overlap in this region.[3]



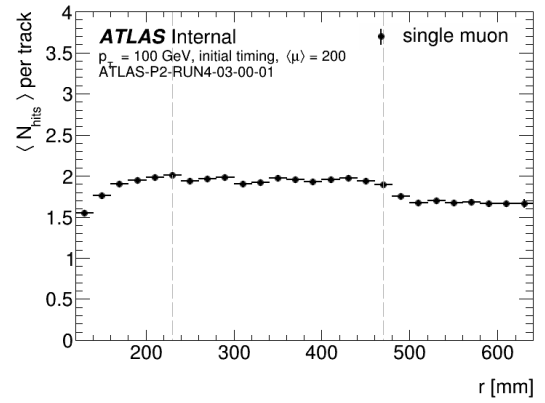
(a)



(b)



(c)



(d)

Figure 23: Mean hit multiplicity per track for prompt and stable muons in the single muon sample with $\langle \mu \rangle = 200$, (a) as a function of x and y , (b) in r without time consistency check and (c), as a function of x and y , (d) in r with time consistency check.

6.2.2 Track-Time Resolution

A track's time resolution is computed as

$$\sigma_{t \text{ track}} = \sqrt{\frac{1}{\sum_{i=1}^{N_{\text{hits}}} 1/\sigma_{t_i}^2}} \quad (8)$$

Where σ_{t_i} are the individual hit-time resolutions. Once again, hit-resolution is currently hard-coded to 35 ps, so in practice Equation 8 only adds a scaling factor depending on the number of HGTD hits used to compute track-time N_{hits} ;

$$\sigma_{t \text{ track}} = \frac{\sigma_{t \text{ hit}}}{\sqrt{N_{\text{hits}}}} \quad (9)$$

6.2.3 Track-Time Matching Quality

In a previous study done for the TDR [3], a method of visualising the quality of track-time association was established. Figure 24 shows the fraction of tracks that were assigned a time, the *Time Association Rate*, in $|\eta|$ for a VBF $H \rightarrow \text{invisible}$ sample used in this TDR study. This denotes the fraction of tracks that, after track filtering, get assigned a time. As the categorisation used here will often recur throughout this thesis, it is important to address it in detail.

A track generated in the ITk can be linked to a truth particle from simulation; the same can be said for the hits generated in the HGTD. This means that a track may have a number of HGTD hits truth associated to the same particle that produced the track. These are a track's *Potential Primes* and ideally these are the only hits a track gets matched to. After extrapolation, however, a track may have missed some of the *Potential Primes* or be matched to hits that are not truth associated to it. The fraction of hits matched to a track after extrapolation that are also truth matched to that track is called the *Prime Fraction* of a track. It is computed as

$$\text{Prime Fraction} = N_{\text{primes}}/N_{\text{tot}}, \quad (10)$$

where N_{primes} is the number of HGTD hits matched to a track after extrapolation that are also truth matched to the same truth particle as the track. These are referred to as *prime hits*. N_{tot} is the total number of hits matched to a track. A higher *Prime Fraction* means that the extrapolation was mostly successful, which in turn means that the track-time computed from these hits is likely to be more accurate.

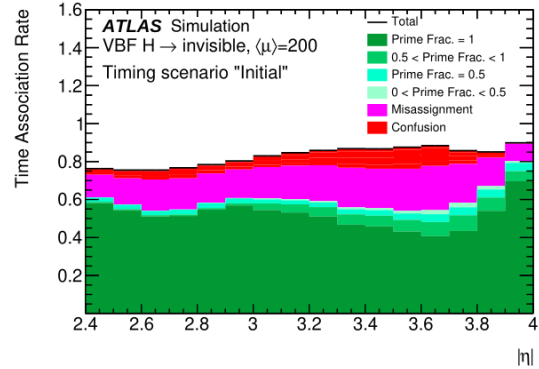
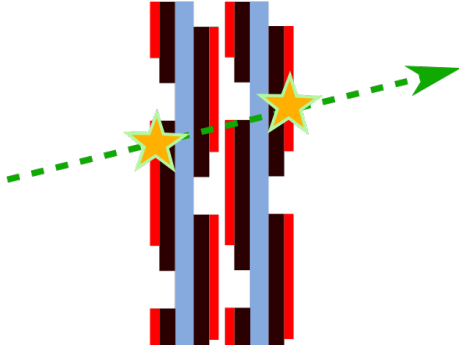


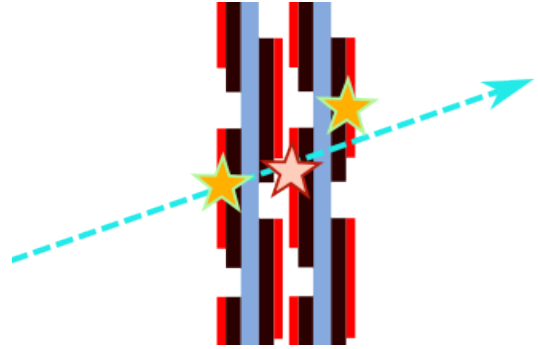
Figure 24: Efficiency plot illustrating the rate of track-to-time association for a VBF $H \rightarrow \text{invisible}$, $\langle\mu\rangle = 200$ sample as a function of $|\eta|$, where the different colours denote track-time quality.

The categories used in Figure 24 are defined as follows:

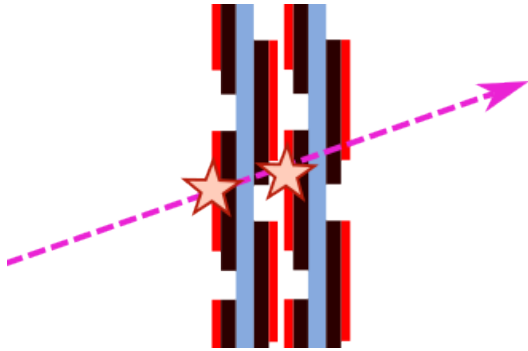
- **Prime Frac. = 1** This means all the HGTD hits matched to a track are correctly assigned. However, it does not account for any prime hits that might have been missed in the extrapolation. One *Prime Frac. = 1* case is illustrated in Figure 25a
- **Prime Frac. = 0.5** For the sake of clarity, Figure 25b illustrates the *Prime Frac. = 0.5* case.
- **Misassignment** This category encompasses all tracks that do not have any prime hits, meaning that based on truth information alone they should not get a time assigned to them, however, they have been matched to at least one HGTD hit nevertheless. See Figure 25c.
- **Confusion** This category includes all tracks that have possible prime hits, but were matched to none of them. Instead these tracks are incorrectly matched to other HGTD hits. See Figure 25d for an illustration.



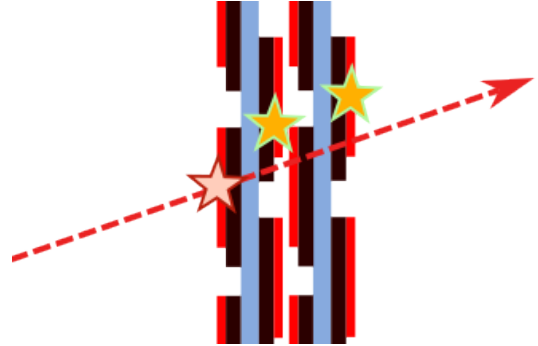
(a) This track is matched to two hits, both being prime hits. The track has no other potential prime hits that the extrapolation missed. This is the ideal scenario of **prime fraction 1**.



(b) This track has two potential prime hits, but is matched to only one of them as well as to another, incorrectly assigned hit. This results in a **prime fraction of 0.5**.

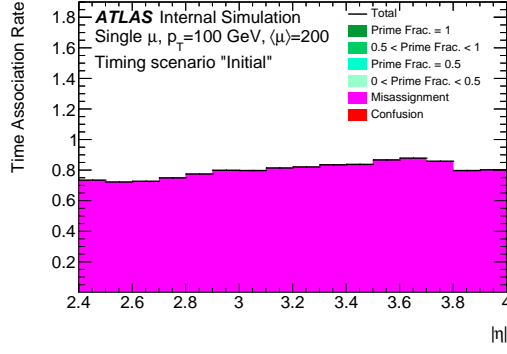


(c) This track has no potential primes, but is nevertheless matched to two hits. It therefore falls in the **Misassignment** category.

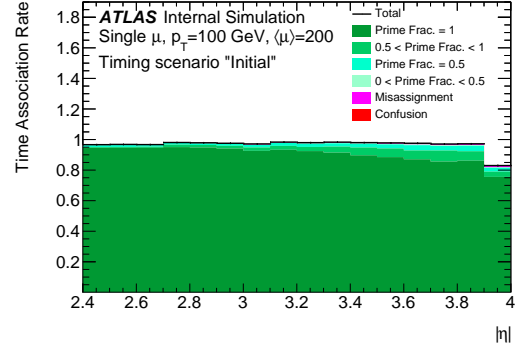


(d) This track has two potential prime hits, but matched to neither of them. Instead it is matched to another unrelated hit. It falls in the **Confusion** category.

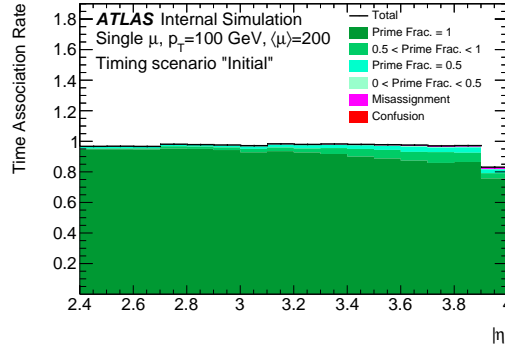
Figure 25: The yellow stars with pale green edges represent potential prime hits. The pale pink stars with red edges represent incorrectly matched hits. If a track passes through a star, that hit was assigned to that track after extrapolation.



(a) No truth-based track-selection.



(b) Truth muons.



(c) Prompt and stable truth muons

Figure 26: Figures comparing the track-time association rate of a $\langle\mu\rangle = 200$ single muon sample with varying track and muons selections. No time consistency check has been applied

6.3 Results

In all results in the following section only tracks that pass $p_T > 1$ GeV and $|\eta| > 2.4$ are considered. Filtering for prompt and stable particles refers to the truth-based selection described in Section 6.1.2.

6.3.1 Muon Selection

Figure 26 shows the effect of matching tracks to truth muons on time association rate without time consistency check for the single muon $\langle\mu\rangle = 200$ sample. Without this truth-matching, the efficiency is dominated by misassigned tracks, i.e. tracks that are matched to HGTD hits during extrapolation, but have no truth-associated prime hits. This is due to the fact that no full truth-level information of the pileup overlay is available in the single muon samples. In other words, the pileup tracks cannot be truth matched to particles because no truth particles are saved in the sample other than those originating from the muon particle gun.

Requiring tracks to be truth matched to muons effectively filters out all non-muon pileup tracks which makes it a fitting approach for studying simulation performance. The time association rate of Figure 26b, consequently represents the fraction of truth muon tracks that get assigned a reconstructed track-time.

As reasoned in Section 6.1.2, secondary particles that have undergone or originate from matter interactions in the detector framework should be filtered out. Comparing Figure 26b and 26c shows that the overall time association rate is barely affected by filtering for prompt and stable muons compared to only the truth-muon selection. Figure 27 compares the efficiency of muon tracks passing the prompt and stable selection compared to the efficiency of timed prompt and stable muons. It shows that approximately 5% of muons are filtered out consistently over $|\eta|$, both with and without timing requirement; non-prompt and unstable muons are equally likely to be assigned a time as prompt and stable ones, which explains the minimal change between Figure 26b and 26c.

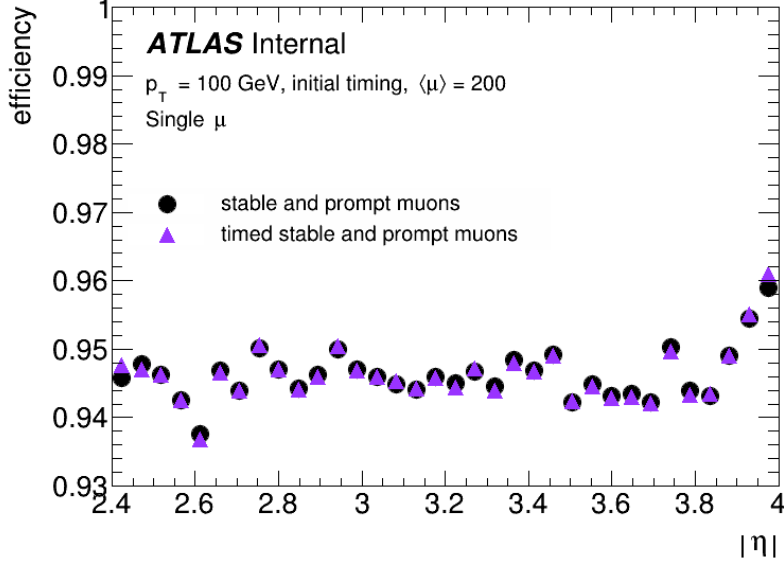


Figure 27

6.3.2 Track-Time Association Quality

To assess more concretely the quality of track-time reconstruction aside from the categorisation described in Section 6.2.3, Figure 30 shows the difference between a muon track's reconstructed time and its truth time for the single muon samples without time consistency check. As the pileup increases, the distribution of $t_{\text{reco}} - t_{\text{truth}}$ becomes wider. Even tracks in the Prime Frac. = 1 category, for which the ITk-to-HGTD extrapolation was successful, can have a large $t_{\text{reco}} - t_{\text{truth}}$. The standard deviation of the $t_{\text{reco}} - t_{\text{truth}}$ distribution of the $\langle\mu\rangle = 0$ sample, $\sigma(t_{\text{reco}} - t_{\text{truth}})_{\langle\mu\rangle=0}$, is 40 ps. Plotting p_T against $|\eta|$ for tracks with $|t_{\text{reco}} - t_{\text{truth}}| > 3 \times \sigma(t_{\text{reco}} - t_{\text{truth}})_{\langle\mu\rangle=0}$ shows that these are mostly low- p_T , high- $|\eta|$ tracks (see Figure 29a).

The time consistency check described in Section 6.2.1 filters out many of these outlier tracks such that track-time association quality in the $\langle\mu\rangle = 200$ sample resembles the $\langle\mu\rangle = 0$ sample more closely (see Figure 30), but some outliers still remain. Comparing Figure 29a and 29b shows that primarily high- p_T tracks get filtered out by the time consistency check and Figure 31 shows that the remaining outliers are mostly matched to only one or two HGTD hits. Therefore, temporal outlier tracks after the time consistency check are likely low- p_T tracks for which the straight-line approximation described in Section 5.2.4 failed or that were mismatched to HGTD hits due to the high degree of pileup.

Figure 31b and 31d show the σ values of Gaussian fits of the $t_{\text{reco}} - t_{\text{truth}}$ distributions for tracks with 1, 2, 3 and 4 HGTD hits separately. Both with and without the time consistency check, they are close to theoretical track-time resolution of Equation 9, i.e. $\sigma_{\text{hit}}/\sqrt{N_{\text{hits}}}$.

6.3.3 Pileup vs Track-Time Efficiency

Figure 32 shows the change in track-time matching efficiency, or *Time Association Rate*, in the single muon samples with different degrees of pileup. In each of these cases, only prompt and stable truth-matched muon tracks are considered. The track-times were computed without applying a time compatibility check. The overall time association rate is minimally affected by pileup HGTD hits. The dip in efficiency at high $|\eta|$ is due to a low rate of sensor overlap close to the beam pipe (see Section 3.1). The overall quality of the track-time association does deteriorate at high $|\eta|$; the lower Prime Fraction shows the increased rate at which tracks are matched to incorrect hits.

As shown in Figure 33, applying the time consistency check as described in Section 6.2.1 causes a decrease in overall track-time matching efficiency, especially in the high- $|\eta|$ region. This is due to the requirement of tracks within $3.5 < |\eta| < 3.9$ to be matched to at least two HGTD hits in the ITk-to-HGTD extrapolation.

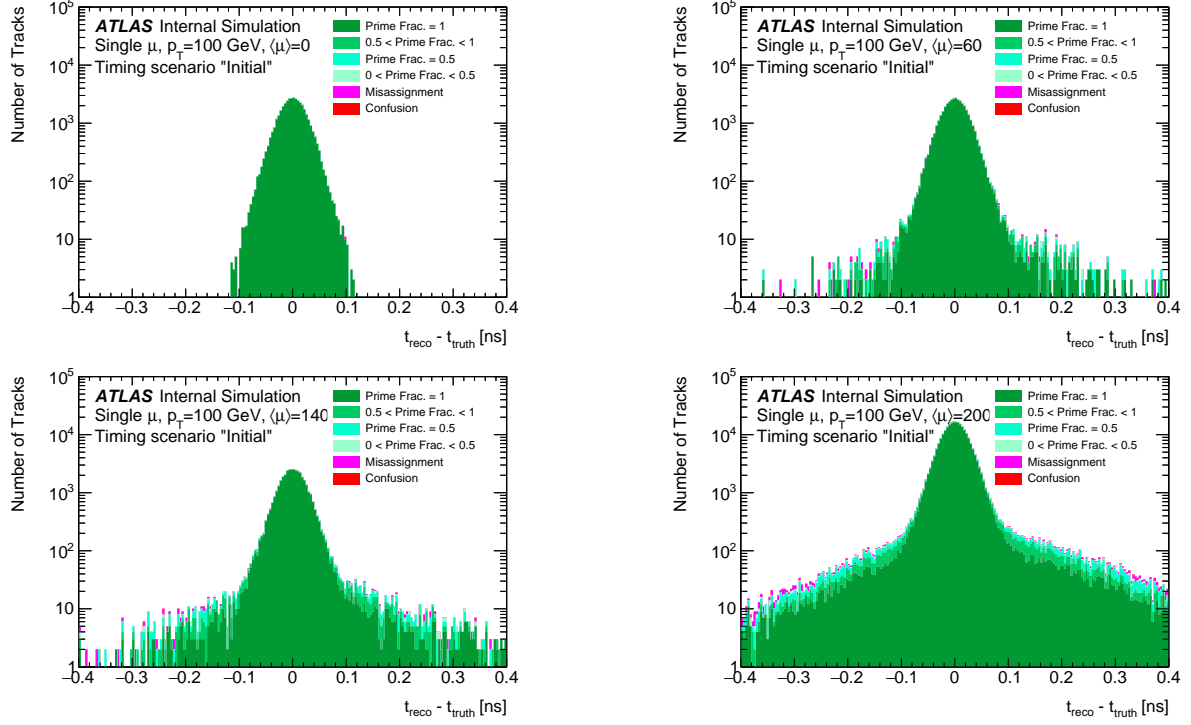


Figure 28: Distribution of the difference between a muon track's truth time and reconstructed time for single muon samples with varying degrees of pileup, filtered for prompt and stable truth muons. No time consistency check was applied.

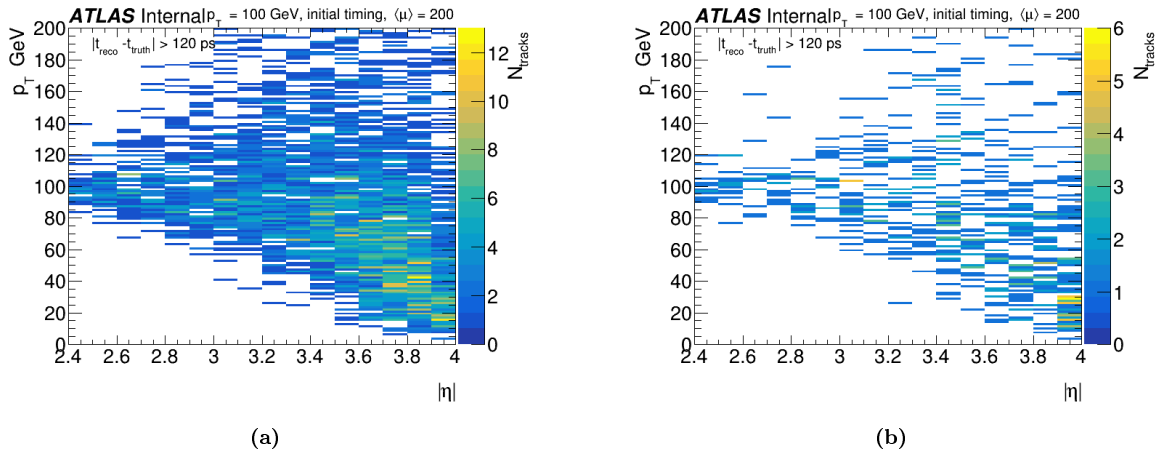


Figure 29: p_T against $|\eta|$ for prompt and stable truth muons with $|t_{\text{reco}} - t_{\text{truth}}| > 120$ ps for the single muon $\langle\mu\rangle = 200$ sample (a) without and (b) with time consistency check.

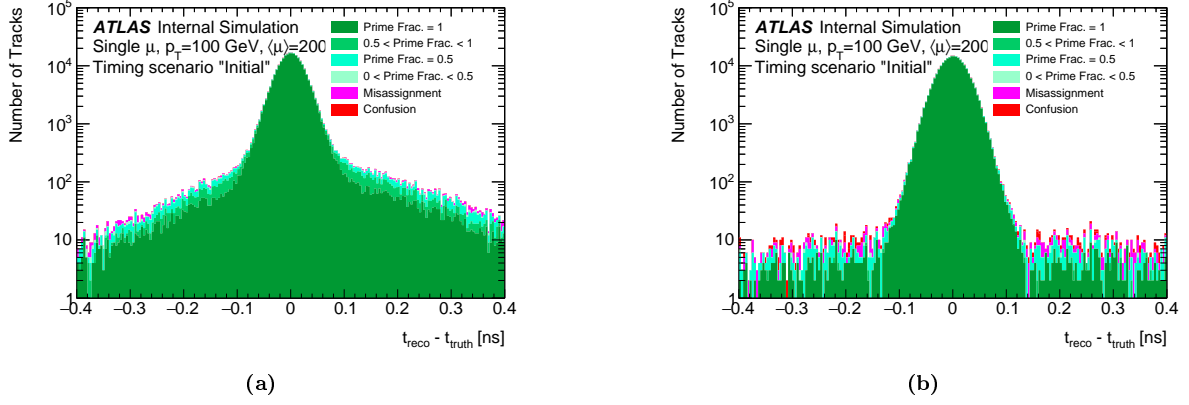


Figure 30: Distribution of the difference between a muon track's truth time and reconstructed time for the single muon $\langle\mu\rangle = 200$ sample filtered for prompt and stable truth muons, (a) without time consistency check and (b) with time consistency check.

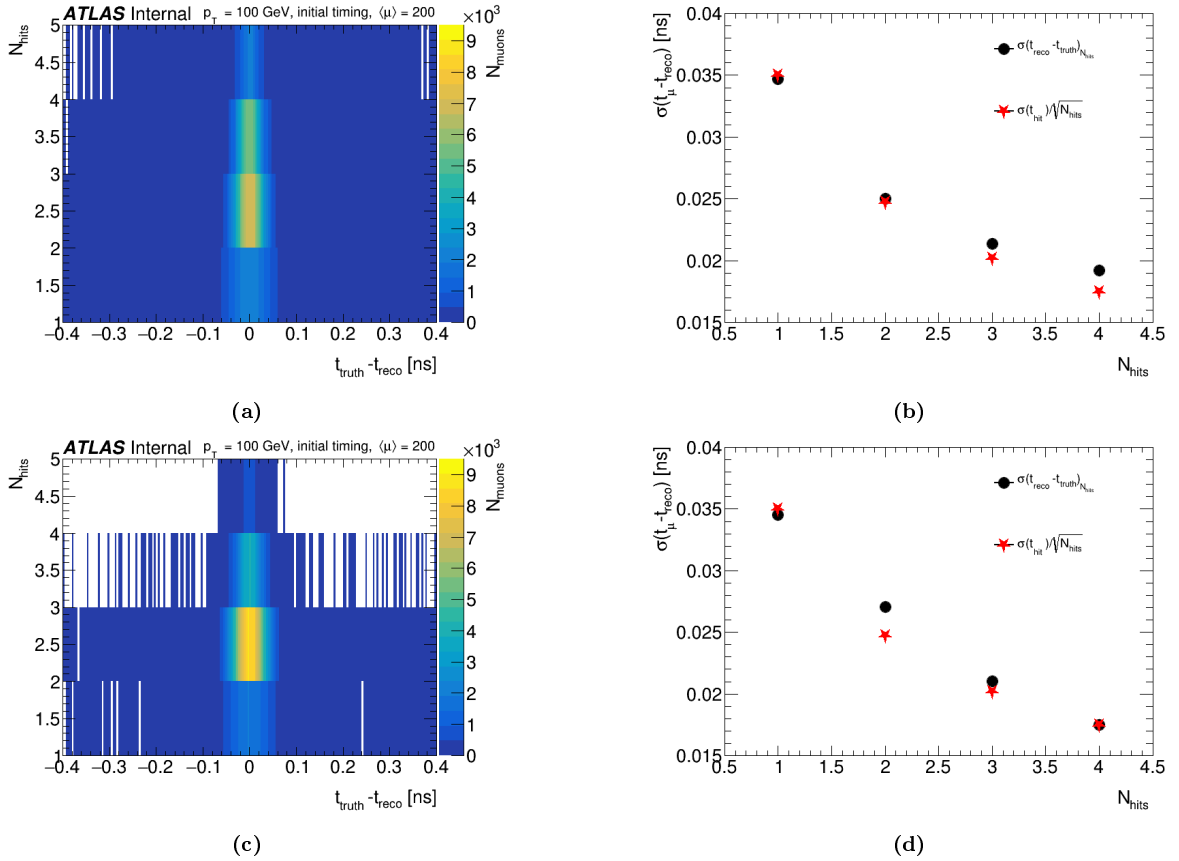


Figure 31: (a) The distribution of $t_{\text{truth}} - t_{\text{reco}}$ for the $\langle\mu\rangle = 200$ single muon sample against the number of HGTD hits used to compute the track-time after applying the time consistency check and filtering for prompt and stable truth muons. (b) The corresponding covariances compared to the expected track-time resolution computed as Equation 9. σ_{hit} is set to 35 ps.

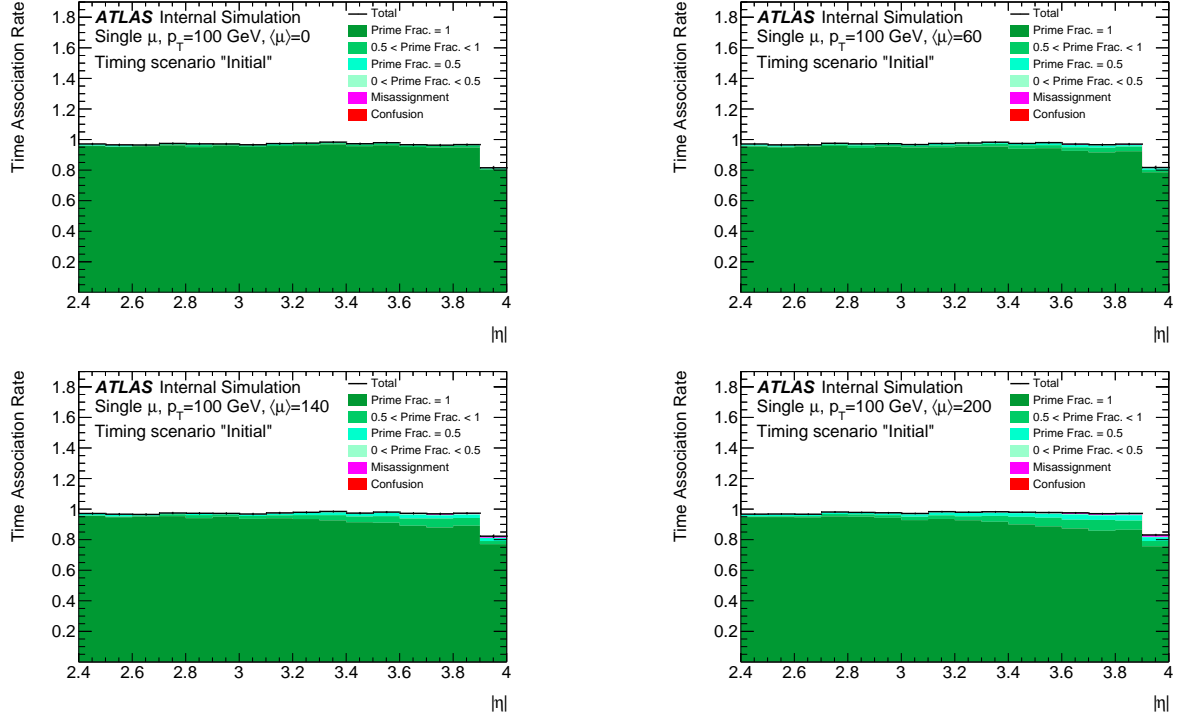


Figure 32: Time association rate for single muon samples with varying degrees of pileup. Filtered for prompt and stable truth muons without time consistency check.

Tracks in this region that are only associated to a single HGTD hit are therefore not assigned a time after the time compatibility check. Notably, the overall quality of track-time association is improved as lower-prime-fraction tracks are filtered out entirely or their wrongly assigned outlier hits are discarded. The quality of track-time reconstruction takes priority over time association efficiency, which justifies this decrease.

6.3.4 Pileup Track-Time

Since the $Z \rightarrow \mu\mu$ samples do have full truth records, the track-time matching quality of pileup and non-muon hard-scatter particles can be assessed. This is important for real world applications of track-time. Figure 34 shows the time association rate for the $Z \rightarrow \mu\mu$ $\langle\mu\rangle = 200$ sample with varying track and muon selections. The prompt and stable truth muon performance resembles the single muon case, but a significant part of the non-muon tracks fall either in the *misassignment* or *confusion* categories. Comparing 34a and 34b shows that unstable and non-prompt particles are likely to be wrongly assigned

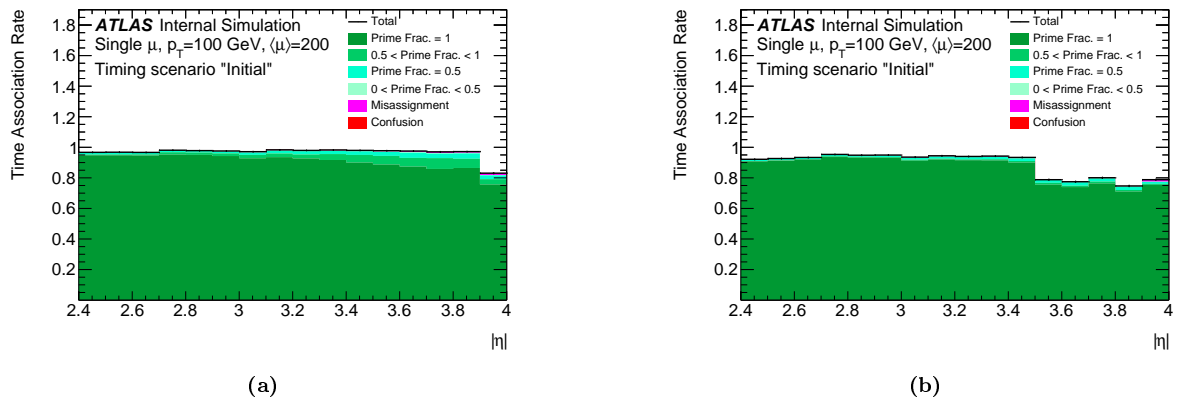


Figure 33: The time association rate for prompt and stable truth muons in the $\langle\mu\rangle = 200$ sample, (a) without and (b) with time consistency check.

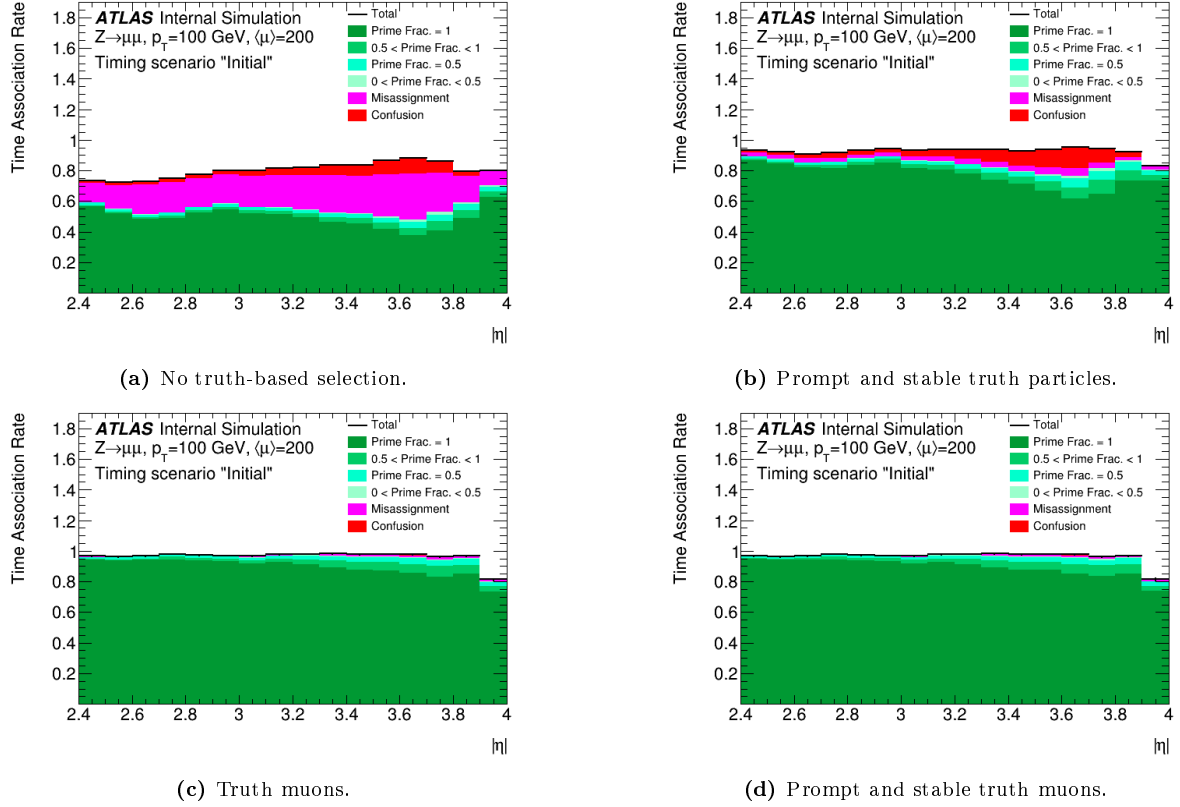
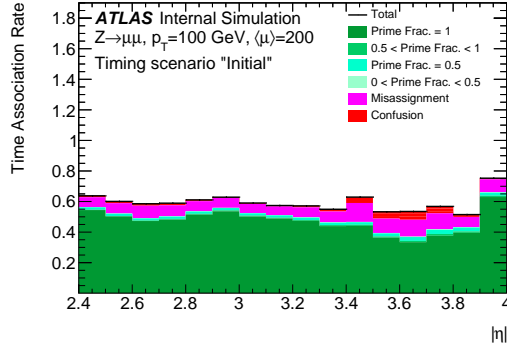


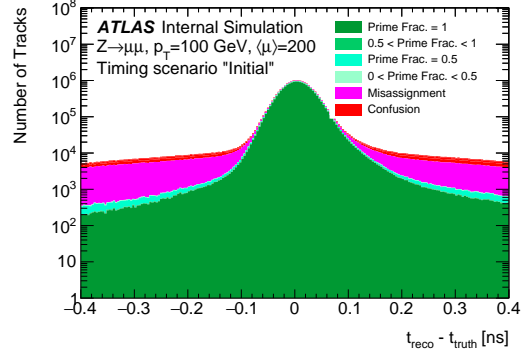
Figure 34: Figures comparing the time association rate of a $\langle\mu\rangle = 200$ $Z \rightarrow \mu\mu$ sample for varying track and muon selections. No time consistency check has been applied

a time (*misassigned*). Stable and prompt non-muon tracks are more likely to be matched to the wrong HGTD hits (*confusion*). The rate of *confusion* is especially high in the $3.5 < |\eta| < 3.9$ range where there is a high pileup rate and a large degree of sensor overlap.

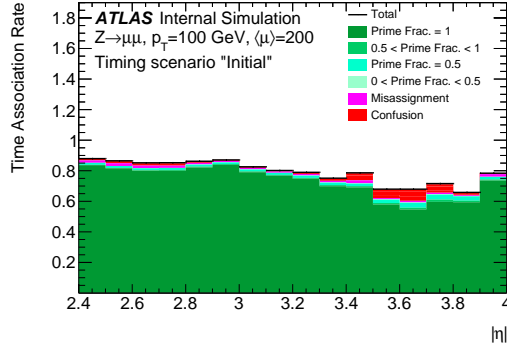
The time consistency check filters out some of the misassigned and confused tracks (see Figure 35). However, after filtering for prompt and stable truth particles, confused tracks remain (Figures 35c and 35d). These bad ITk-to-HGTD extrapolations result in large difference between reconstructed and truth track-time. Combining the time consistency check with the selection for prompt and stable muons results in similar performance to the single muon sample; near all *confusion* and *misassigned* tracks are filtered out. This means that the ITk-to-HGTD extrapolation works especially well for muons, but is less successful for the other tracks. The hadronic interactions simulated in these samples give rise to wide arms in the $t_{\text{reco}} - t_{\text{truth}}$ -distributions even in the $\langle\mu\rangle = 0$ sample case (see Figure 36). The straight-line approximation for the time-of-flight correction causes to a slight asymmetry in the arms of these distributions as some particles travel a longer path.



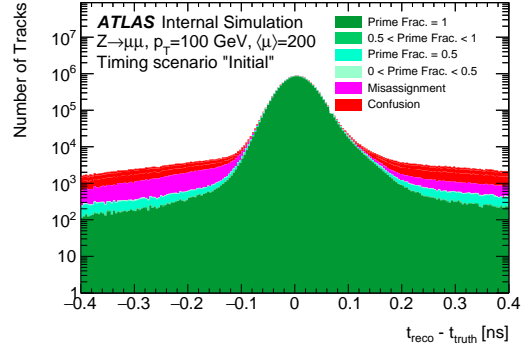
(a) No truth-based selection.



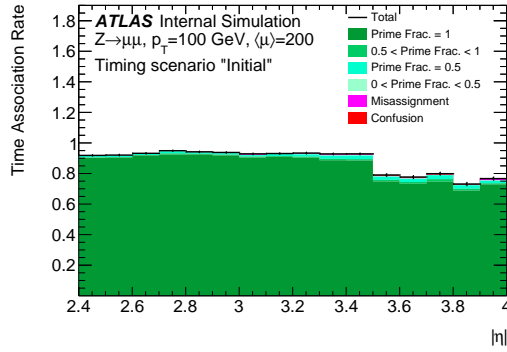
(b) No truth-based selection.



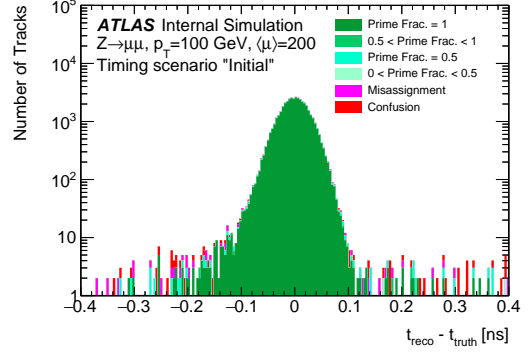
(c) Prompt and stable truth particles.



(d) Prompt and stable truth particles.

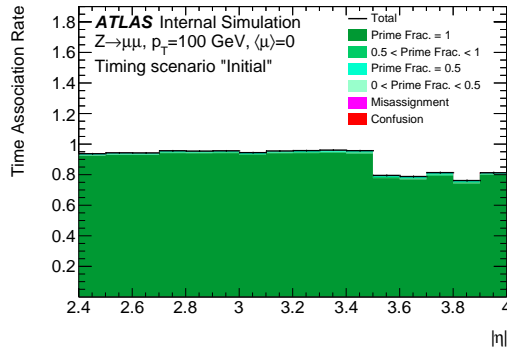


(e) Prompt and stable truth muons.

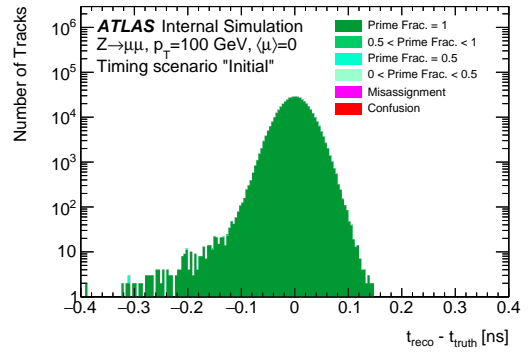


(f) Prompt and stable truth muons.

Figure 35: The time association rates as functions of $|\eta|$ and $t_{\text{reco}} - t_{\text{truth}}$ -distributions of the $Z \rightarrow \mu\mu$ sample with $\langle\mu\rangle = 200$ with varying track and muon selections.



(a)



(b)

Figure 36: (a) The time association rate as function of $|\eta|$ and (b) $t_{\text{reco}} - t_{\text{truth}}$ -distributions of the $Z \rightarrow \mu\mu$ sample with $\langle\mu\rangle = 0$. The sample was filtered for prompt and stable truth muons and the time consistency check was applied.

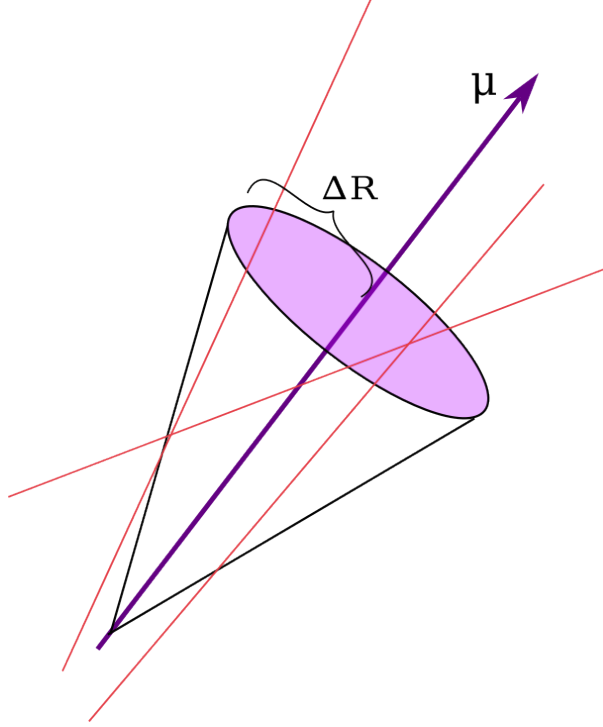


Figure 37: Schematic of the isolation cone around a muon track.

7 Muon Isolation

In Section 6.1.2 a method for filtering secondary, non-prompt particles is discussed that uses truth information to identify stable and prompt muons. While this is an acceptable approach when assessing simulation performance, it is not applicable when working with real data. Instead, muons are identified through reconstruction as described in Section 4.4 and *isolation variables* are used to reject background contributions of muons produced in secondary interactions such as light and heavy hadron decays. These variables are measures for detector activity around a particle and can be either track- or calorimeter-based.[13] Since current methods for track-time association are entirely track-based, this thesis is also limited to track-based isolation. In the following, the effect of track-time cuts on these isolation variables is studied.

7.1 Isolation Variables

Track-based isolation variables are typically quantified in terms of the summed transverse momentum of all tracks that fall within a cone in $\eta - \phi$ space around the original particle (see Figure 37). This cone, in its simplest form, is defined as

$$\Delta R = \sqrt{\Delta\eta^2 + \Delta\phi^2} \quad (11)$$

With $\Delta\eta = \eta_{\text{core}} - \eta_{\text{track}}$ and $\Delta\phi = \phi_{\text{core}} - \phi_{\text{track}}$. In this thesis, only the tracks' defining parameters (see Section 4.2) are used to compute this variable. The core is defined depending on the type of particle for which the isolation is being computed; in the case of muons, only a single muon track is counted as the core.[18]

The summed transverse momentum of all tracks around a particle that fall into a cone is called the p_T -cone value. The typical cone sizes, i.e. the max allowed ΔR , used to compute this variable are 0.2, 0.3 and 0.4, referred to as *ptcone20*, *ptcone30* and *ptcone40* respectively. The core's p_T is excluded from these sums.

In some cases, a slight variation to this approach is taken. Instead of using a constant value for the maximal p_T -cone radius, tracks must fall within a cone of size

$$\Delta R = \min \left(\frac{k_T}{p_T}, R \right) \quad (12)$$

where k_T is constant set to 10 GeV, p_T is the transverse momentum of the core particle and R is the maximal cone radius, i.e. 0.2, 0.3 or 0.4. This translates to a narrower isolation cone for high- p_T tracks. The isolation variables computed this way are called the variable p_T -cone value, or *ptvarcone*. As mentioned, isolation variables are used to filter out non-prompt muons. This is done by setting a maximum value of $pt(var)coneXX/p_T$, where p_T is once again the core particle's transverse momentum and $XX \in 20, 30, 40$. Weighting the cut by p_T accounts for higher pileup rates around low- p_T muons.[18] The Muon Combined Performance Working Group [19] typically provide recommended cuts in terms of this variable. Whether the constant or variable cone size is used depends on the particle type. For Run 3, the recommended "Loose" track-based isolation working point for muons is

$$ptvarcone30/p_T < 0.15 \quad (13)$$

If a muon does not pass this cut after pileup filtering, the tracks in its cone are likely from hadrons and the muon was likely produced in a secondary hadronic decay.[13]

7.2 Track Selection

The same base-line kinetic cuts used for the track-time association study as described in Section 6.1, i.e. $p_T < 1$ GeV and $|\eta| > 2.4$, were used to study isolation. Instead of using truth matching to filter out pileup, additional kinetic and detector hit count based track selections were applied before computing the p_T -cones. As of the writing of this thesis, there is no recommended ITk cut working point available. Instead, a "Loose" cut level was used similar to the cuts used for ITk track reconstruction in [20]. Table 3 summarises the track cuts used for computing the isolation variables.

7.2.1 Track-to-Vertex Association

Another approach to pileup filtering is to use spatial cuts to test a track's physical nearness to the hard-scatter vertex (also referred to as the *primary vertex*). Typically, a track-to-vertex association tool is used when computing isolation variables that checks whether a track has been used in a vertex reconstruction as described in Section 4.3. The tracks' weights from this reconstruction are then used to filter out tracks most likely originating from pileup vertices. All other tracks must satisfy

$$\begin{aligned} |\Delta z \sin \theta| &< 5 \text{ mm} \\ |d_0| &< 5 \text{ mm.} \end{aligned} \quad (14)$$

Here $|\Delta z \sin \theta|$ is the distance between the primary vertex and the tracks defining parameter coordinate. d_0 is the track's defining transverse impact parameter.[18]

7.3 Adding Timing

Particles originating from the same vertex typically consistent in time. Particles from hadronic decays are likely to be surrounded by other particles from the same decay, while prompt muons from bosonic decays are likely more isolated.[13] This provides a possibility to improve pileup filtering and isolation with track-time cuts. In a previous study [21] on tracking isolation of forward electrons using track-timing, the following variable was introduced to apply time cuts during the computation of isolation variables:

$$\frac{\Delta T}{\sigma} = \frac{t_\mu - t_{\text{cone track}}}{\sqrt{\sigma_{t_\mu}^2 + \sigma_{t_{\text{cone track}}}^2}} \quad (15)$$

Variable	"Loose" Cuts
$ \eta $	< 4
N_{Si}	≥ 8
N_{hole}^{Si}	≤ 2
N_{hole}^{Pix}	≤ 1
p_T	$\geq 1 \text{ GeV}$
$ z_0 \sin \theta_0 $	$< 3 \text{ mm}$

Table 3: The "Loose" selection cuts to track parameters and detector hit counts used for the muon isolation pileup filtering. N_{Si} refers to a track's number of hits in the all-silicon ITk, N_{hole}^{Si} is the number of holes in the ITk where a hit is expected based on the particle trajectory but not measured and N_{hole}^{Pix} is the number of holes in the Pixel sub-detector.

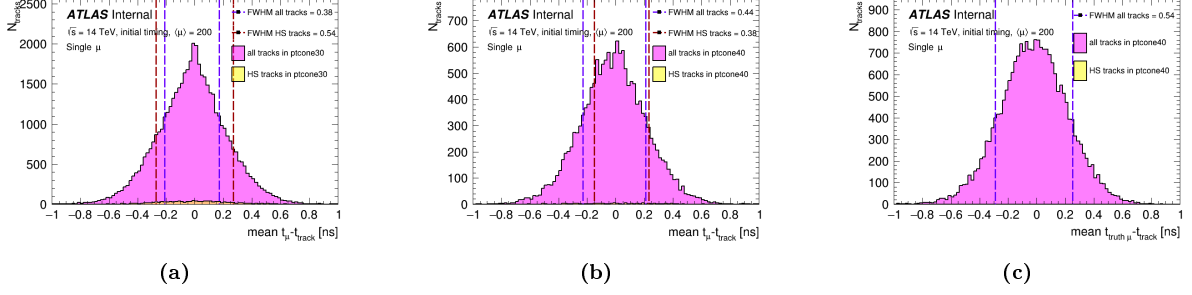


Figure 38: Mean $t_\mu - t_{\text{track}}$ in a $R = 0.3$ cone for the $\langle\mu\rangle = 200$, single muon sample with (a) no upstream muon quality control, (b) all "VeryLoose" muons filtered out and (c) only truth muons. The "all tracks in ptcone30" category are muons containing any timed tracks within the $R = 0.3$ cone. "HS tracks in ptcone30" category only contains truth associated, timed, hard-scatter tracks in the $R = 0.3$ cone. The vertical, dashed lines indicate the Full Width Half Maximum of these distributions.

Where t_μ is the time associated with a muon via the track-time matching procedures described in Section 6.2. $t_{\text{cone track}}$ is the reconstructed time of a track within a given isolation cone around the muon. σ_{t_μ} and $\sigma_{t_{\text{cone track}}}$ are the corresponding track-time resolutions, computed using 8.

7.4 Muon Selection

As described in Section 4.4 there are several ways in which a muon may be reconstructed from (simulated) detector output. Since track-time association is track-based, only muons that were reconstructed with an ITk track are considered. The quality of reconstruction is defined using predefined WPs as described in Section 4.4. In order to optimise muon identification efficiency, this thesis uses the "Loose" working point. Figure 38a shows the distribution of the mean $\Delta T = t_\mu - t_{\text{track}}$ in a cone of radius $R = 0.3$ per muon for the $\langle\mu\rangle = 200$ particle gun sample, without any upstream muon quality control. The irregular shape hints at a significant contribution of poorly reconstructed muons. In Figure 38b the "VeryLoose" muons are filtered out, i.e. the "Loose" muon WP. Comparing this to 38c, which only contains truth muons without any reconstruction quality filters applied, suggests that this selection is strict enough to significantly improve results.

7.5 Results

For all results in this section tracks are filtered for $p_T > 1$ GeV and $|\eta| > 2.4$ and the cuts of Table 3. The "Loose" muon reconstruction WP is used. Track-time is computed with the time consistency check procedure.

7.5.1 Track-Time Quality

The truth-based selections for prompt and stable muons used to study track-time association cannot be used in the same way to study the effect of time-cuts on isolation variables since truth-based selections are not applicable to real-data analyses. The track-time matching efficiency and the $t_{\text{reco}} - t_{\text{truth}}$ -distributions of the $Z \rightarrow \mu\mu$ samples with only base-line kinetic cuts are plotted in Figure 39. This shows that a significant fraction of timed tracks have been assigned a time mistakenly and fall in the *misassigned* category, both for the $\langle\mu\rangle = 200$ and $\langle\mu\rangle = 0$ samples. As discussed in Section 6.3.4, these are likely from unstable and non-prompt particles from hadronic decays. Figure 40 shows the distribution of $\Delta T/\sigma$ of tracks within the variable p_T -cone with max radius $R = 0.3$ for the $Z \rightarrow \mu\mu$ samples. The quality of track-time reconstruction of the tracks within this cone is categorised as defined in Section 6.2.3. As expected from Figure 39, the majority of these tracks are either *misassigned* or fall in the well-reconstructed Prime Frac = 1 category. The *misassigned* track-times may be near the muon core-track in time if for example, a track that is spatially near the muon was mistakenly assigned an HGTD hit originating from the muon or another hard-scatter particle. Hence, time-cuts are not effective for filtering out pileup with wrongly assigned times.

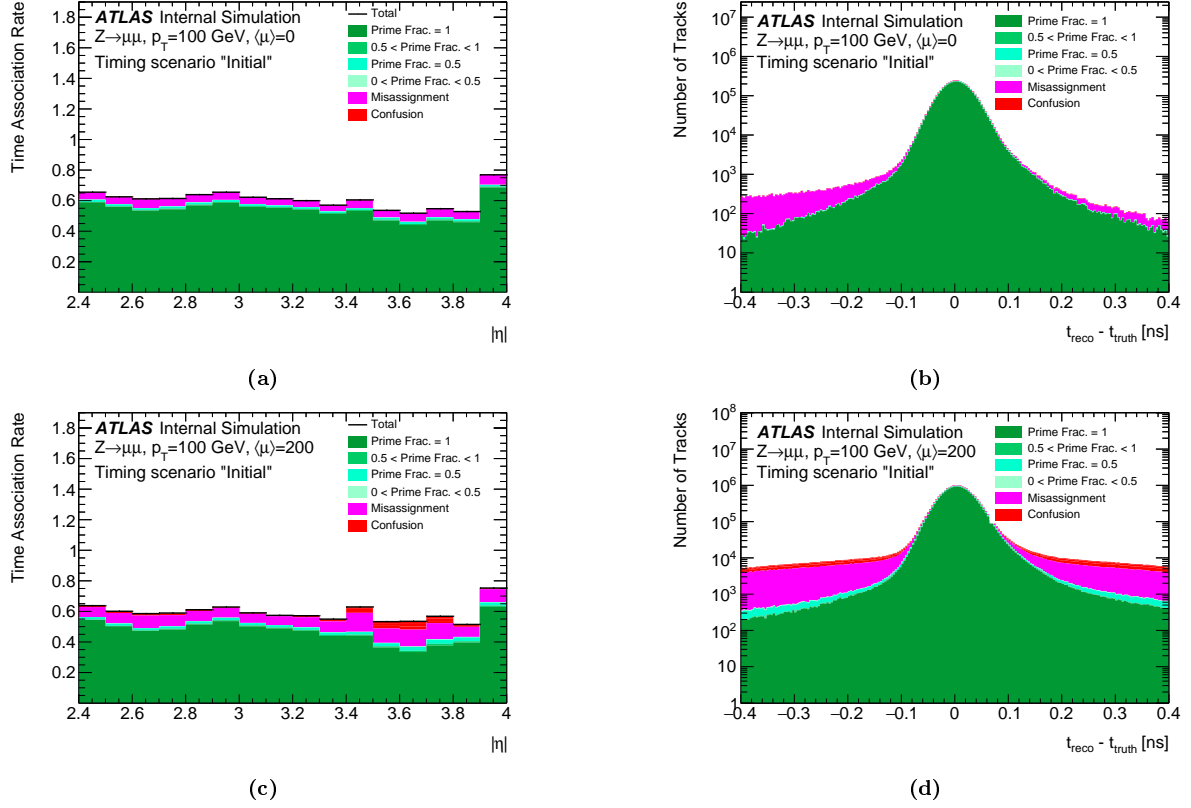


Figure 39: The track time association rate in $|\eta|$ and $t_{\text{reco}} - t_{\text{truth}}$ -distributions of the $Z \rightarrow \mu\mu$ samples with (a), (b) $\langle \mu \rangle = 0$ and (c), (d) $\langle \mu \rangle = 200$.

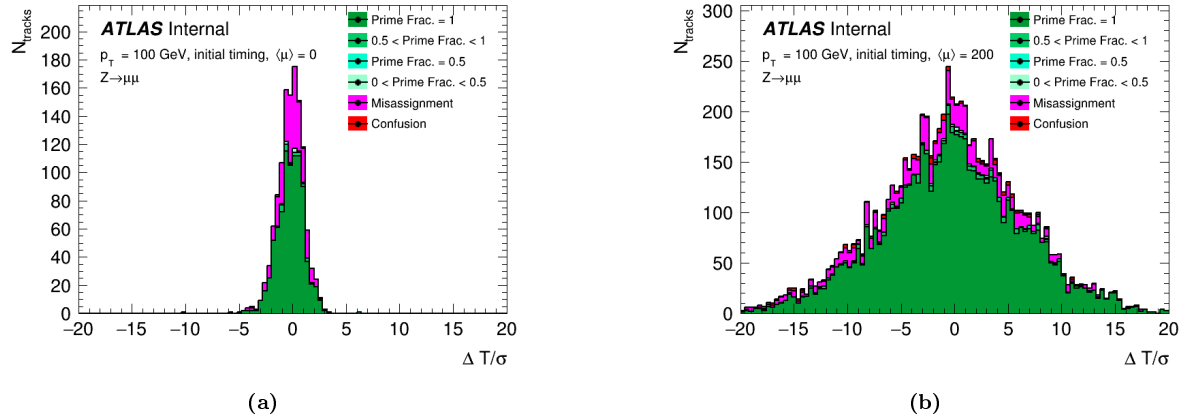


Figure 40: $\Delta T/\sigma$ distribution of tracks in a variable p_T -cone of maximal radius $R = 0.3$ for the $Z \rightarrow \mu\mu$ samples of (a) $\langle \mu \rangle = 0$ and (b) $\langle \mu \rangle = 200$ samples with track-time reconstruction quality of the cone-track categorised as in Section 6.2.3.

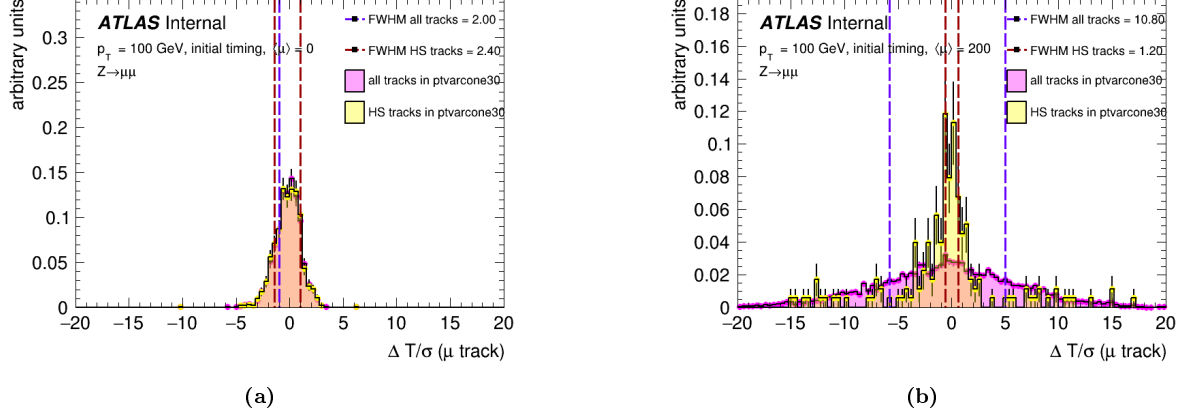


Figure 41: Normalised distribution of tracks in a variable isolation cone with max radius $R = 0.3$ for the $Z \rightarrow \mu\mu$ samples with (a) $\langle\mu\rangle = 0$ and (b) $\langle\mu\rangle = 200$. For the "all tracks in ptvarcone30" category, all tracks that passed track selection were counted while for the "HS tracks in ptvarcone30" an additional truth matching of tracks to the hard-scatter vertex was applied. The distributions of these categories are normalised separately in order to compare their shape. The dashed lines indicate the edged of the Full Width Half Maximum of both categories.

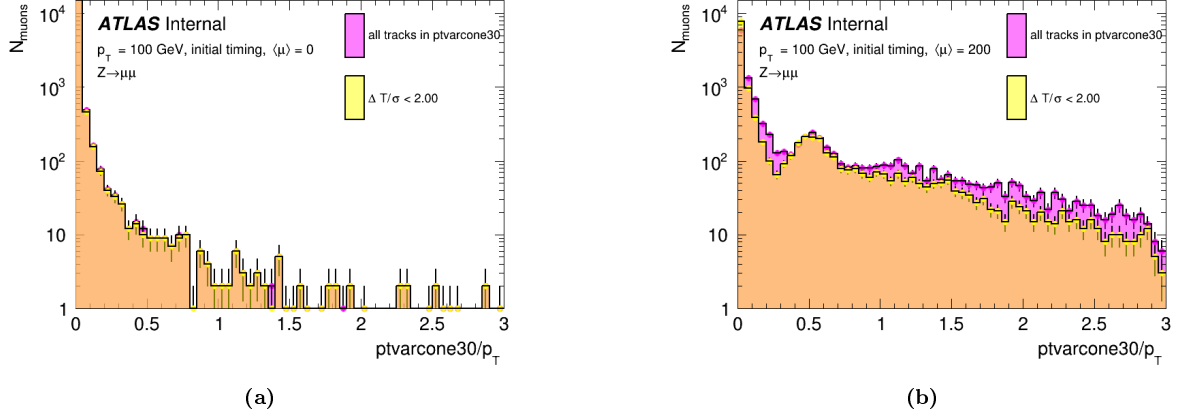


Figure 42: Distribution of $ptvarcone30/p_T$ with and without a $\Delta T/\sigma < 2.00$ cut, for the $Z \rightarrow \mu\mu$ samples with (a) $\langle\mu\rangle = 0$ and (b) $\langle\mu\rangle = 200$.

7.5.2 Nominal Time-Cut

Figure 41 shows the $\Delta T/\sigma$ distributions of tracks in the variable p_T -cone with maximal radius $R = 0.3$ for the $Z \rightarrow \mu\mu$ samples with and without pileup. When considering all tracks in this cone, the $\Delta T/\sigma$ distribution of the $\langle\mu\rangle = 0$ sample has a Full Width Half Maximum (FWHM) of 2.00 compared to the pileup case with FWHM = 10.80. This suggests that tracks with $|\Delta T/\sigma| > 2.00$ in the $\langle\mu\rangle = 200$ sample are likely pileup contributions. The central peak of the $\Delta T/\sigma$ distribution of truth-matched hard-scatter tracks in the $\langle\mu\rangle = 200$ sample confirms this (Figure 41b). $|\Delta T/\sigma| < 2.00$ is therefore taken as a nominal time-cut. Figure 42 shows the effect of this cut on the $ptvarcone30/p_T$ variable. As expected, there is minimal change in the $\langle\mu\rangle = 0$ sample, but the $\langle\mu\rangle = 200$ sample is significantly affected especially for high- $ptvarcone30/p_T$ muons.

7.5.3 Isolation Efficiency

Figure 43 shows the impact of the $|\Delta T/\sigma| < 2.00$ cut on the isolation efficiency of the $Z \rightarrow \mu\mu$ samples, defined here as the fraction of reconstructed muons that passes a given $ptvarcone30/p_T$ cut. Comparing Figure 43a and 43b shows that the time-cut improves isolation efficiency toward the zero-pileup performance. To quantify the effect of varying time-cuts on muon isolation, the Run 3 recommended loose cut on track-based isolation variables, $ptvarcone30/p_T < 0.15$ [19], was chosen as a base-line. Figure 44

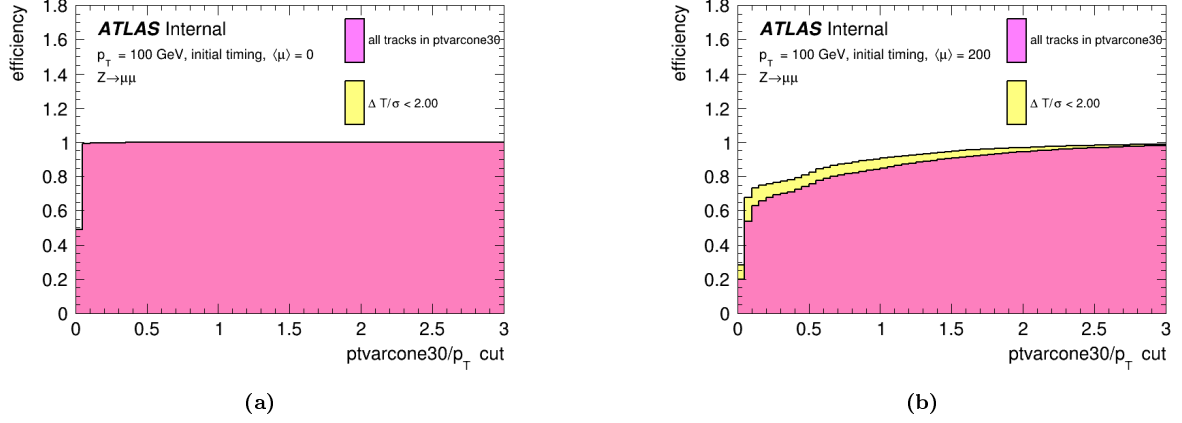


Figure 43: The efficiency of muons passing a $ptvarcone30/p_T$ cut with and without a $\Delta T/\sigma < 2.00$ cut, for the $Z \rightarrow \mu\mu$ samples with (a) $\langle\mu\rangle = 0$ and (b) $\langle\mu\rangle = 200$.

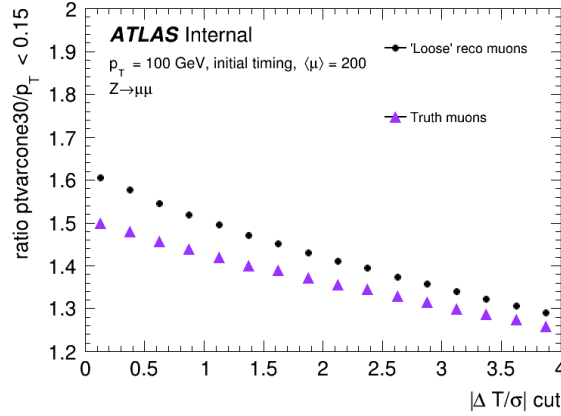
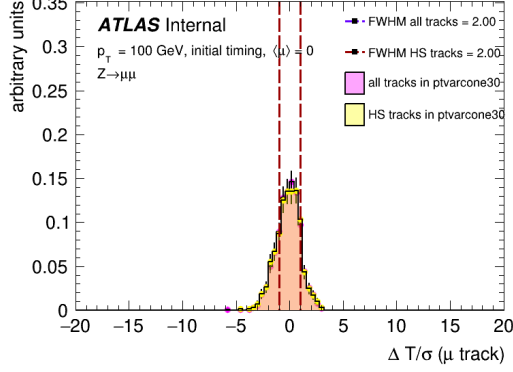


Figure 44: The ratio of reconstructed (black dot) and truth (purple triangle) muons that pass the $ptvarcone30/p_T < 0.15$ cut with time-cut over without time-cut, computed for the $Z \rightarrow \mu\mu$ $\langle\mu\rangle = 200$ sample.

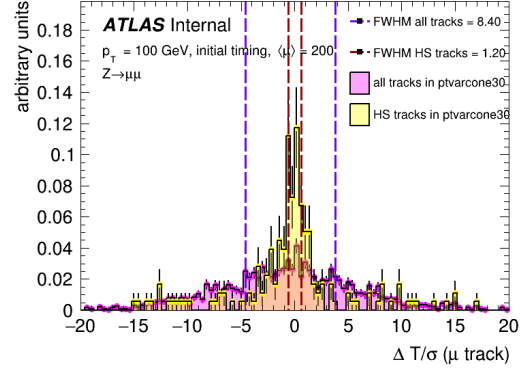
shows that the fraction of muons that pass this isolation cut increases for stricter time-cuts compared to without a time-cut. The fractional increase of truth muons that pass $ptvarcone30/p_T < 0.15$ is less than the fractional increase of the reconstructed muons overall.

7.5.4 Track-To-Vertex-Association

To test if applying a time-cut would have a significant effect when combined with a track-to-vertex association filter as described in Section 7.2.1, the additional cuts of $|\Delta z \sin\theta| < 5$ mm and $|d_0| < 5$ mm were applied (Equations 14). In the $\langle\mu\rangle = 0$ sample, some of the events do not contain an accessible hard-scatter vertex so the track-to-vertex-association cannot be applied. These events are therefore discarded. The resulting $\Delta T/\sigma$ -distributions are shown in Figure 45. As expected, the $\langle\mu\rangle = 0$ is barely affected. $|\Delta T/\sigma| < 2.00$ is once again taken as the nominal time-cut. Figure 46 shows the results of this selection on the $\langle\mu\rangle = 200$ sample. The track-to-vertex association filter significantly improves the isolation efficiency towards the zero-pileup case and the overall effect of the time-cut is diminished. Nevertheless, time-cuts do increase the rate at which muons pass the $ptvarcone30/p_T < 15$ cut by at most approximately 9%.

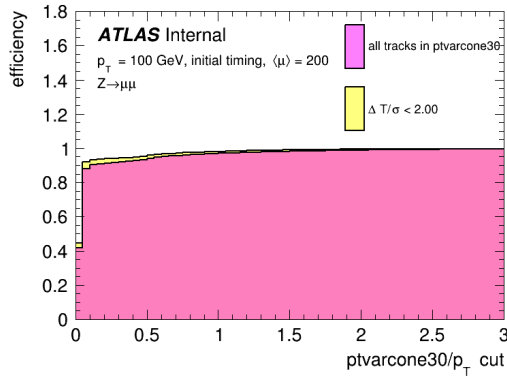


(a)

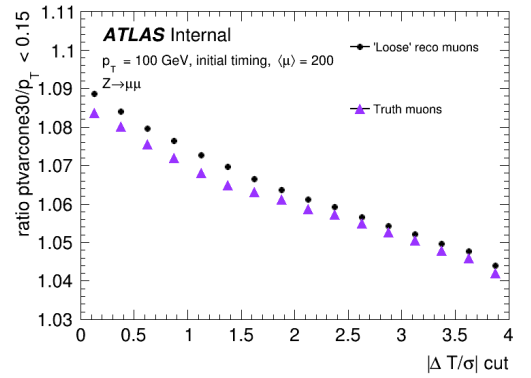


(b)

Figure 45: Normalised distribution of tracks in a variable isolation cone with max radius $R = 0.3$ for the $Z \rightarrow \mu\mu$ samples with (a) $\langle\mu\rangle = 0$ and (b) $\langle\mu\rangle = 200$. For the "all tracks in ptvarcone30" category, all tracks that passed track selection were counted while for the "HS tracks in ptvarcone30" an additional truth matching of tracks to the hard-scatter vertex was applied. The distributions of these categories are normalised separately in order to compare their shape. The dashed lines indicate the edged of the Full Width Half Maximum of both categories.



(a)



(b)

Figure 46: (a) The efficiency of muons passing varying isolation cuts for a $|\Delta T/\sigma| < 2.00$ time-cut with track-to-vertex pileup filtering. (b) The ratios of reconstructed and truth muons that pass $ptvarcone30/p_T < 0.15$ with over without time-cut. Computed with $Z \rightarrow \mu\mu$ sample with $\langle\mu\rangle = 200$.

8 Conclusion and Outlook

Current methods of track-time reconstruction work well for high- p_T truth muons in high-pileup samples, especially when applying a time consistency check to filter out outlier HGTD hits. The standard deviation of $t_{\text{reco}} - t_{\text{truth}}$ distributions separated for HGTD hit-count are in accordance with theoretical values for track-time resolution, i.e. $\sigma_{\text{hit}}/\sqrt{N_{\text{hits}}}$. However, there is still room for improvement toward realistic performance and for non-muon track-time reconstruction. As discussed in Section 6.2.1, the methods used in this thesis for track-time computation use a default hit-time resolution of 35 ps. However, realistically this value should not be static, but instead be dependent on systematic detector errors and the amount of radiation the sensors have undergone. Implementing this would require a detailed model of these errors, which is no easy task, but would improve the predictive ability of the HGTD simulation. The current time consistency check procedure also uses a static χ^2 limit, while typically a limit on χ^2 fit quality is set for $\chi^2/n.d.f.$. This could be an additional point of improvement for track-time computation. Remaining errors in $t_{\text{reco}} - t_{\text{truth}}$ after applying the time consistency check are in part due to the straight-line approximation used to correct HGTD hit time-of-arrival. For low- p_T particles this approximation is reduced in accuracy, which should be compensated for.

The track-time association of pileup and non-muon hard-scatter tracks is less successful than for truth muons. Unstable and non-prompt particles are likely to be mistakenly assigned a time and stable and prompt non-muon particles are relatively likely to be matched to the wrong HGTD hits. This implies that the ITk-to-HGTD extrapolation could still be improved. One possibility for improvement is the use of timing during extrapolation. If a time consistency check could be applied during track fitting, the matching of tracks to HGTD hits could be improved overall. It is important to improve track-time matching for all particle types to optimise the effectiveness of track-time as a tool to improve physics analyses.

It was shown that track-time information can be used to filter out pileup and help achieve muon isolation performance in high-pileup samples such that it approaches the zero-pileup case and improves truth muon isolation efficiency. In combination with a track-to-vertex association selection, the effects of time-cuts are diminished but nevertheless result in an improvement of the muon isolation efficiency. In a future study track-to-vertex-association and time-cuts could be simultaneously fine-tuned to optimise pileup filtering and the signal-to-background ratio. Unfortunately, there were no samples of background muon production processes available for this thesis. Applying the approach used in [21] to muons, which aims to optimise the signal-to-background ratio for forward electrons passing p_T -cone cuts by varying $\Delta T/\sigma$ and $z_0 \sin\theta$ requirements, would be a natural extension of the work presented in this thesis.

It is important to note that current muon reconstruction is only available for tracks in $|\eta| < 2.7$. This greatly limits the extend to which timing info and its effect on track reconstruction and muon isolation can be studied. It might be possible to adopt a simplified ITk track and muon identification approach to extend this range by spatially matching tracks to traces in the muon spectrometer. In [21], for example, the range of forward electrons was extended by matching tracks to calorimeter hits. However, in the future the η -reach of full reconstruction algorithms should be adapted to cover the whole ITk range; as the high- $|\eta|$ range is subject to the highest pileup-track rate, it is simultaneously the least suitable for simplified track-to-muon matching procedures and most crucial in assessing the potential impact of timing on isolation variables.

8.0.1 Outlook

It would be beneficial for future studies to implement an integrated time-based track selection tool that can be used inside the existing isolation tools. The approach used in this thesis when working with isolation tools (specifically [22]) is to build an exclusion set of tracks that do not pass a given time-cut, meaning the track selection is done within the encompassing algorithm instead of in the isolation tool. The main issue encountered when attempting to implement this track-selection within an isolation tool was the fact that when the Athena package that facilitates track-time computation [23], computes a track's time it decorates the track particle object. This is a fundamentally non-constant operation, but track selection tools within Athena explicitly require the use of only constant functions; an object that must either pass or not pass a certain selection must not be changed during this process. A solution to this would be to compute track-time in an earlier step of the simulation and reconstruction process such that it is a variable accessed by a member function of the track-particle class. This can only be

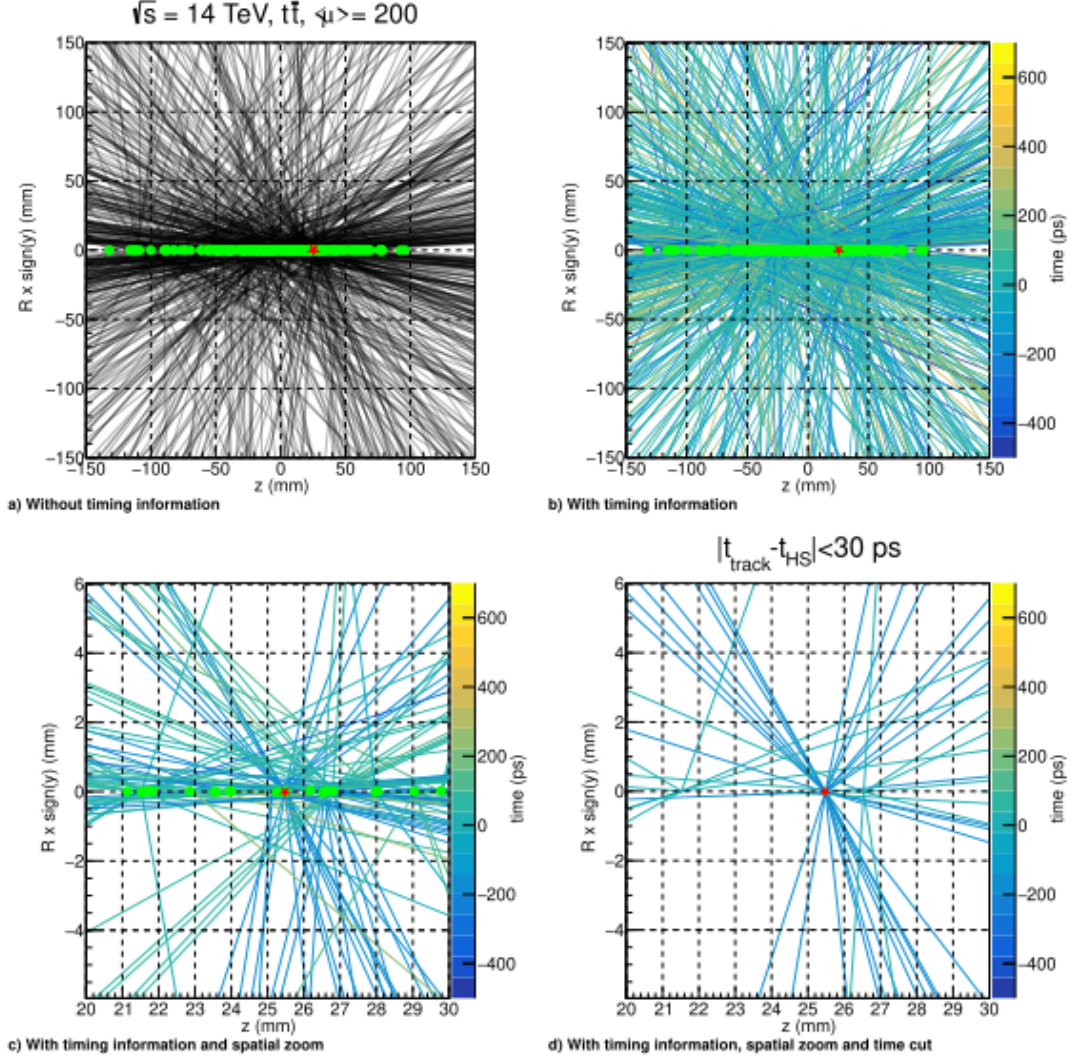


Figure 47: Illustration of the effect of spatial and temporal cuts on track selection for vertex identification. Generated with a $\langle\mu\rangle = 200$ $t\bar{t}$ sample. Track-time is randomly assigned from a Gaussian distribution to mimic as no full simulation is available.

implemented once methods for track-time association are more mature.

The HGTD will be installed as the first timing detector in ATLAS for the HL-LHC. Research and development is well underway, but looking further into the future there are plans to expand ATLAS's timing reach to cover the full η -range of the ITk and develop four-dimensional tracking where time is used to improve track reconstruction. Figure 47 illustrates how timing information for all tracks can help clean up pileup interactions. These plots present the possibilities of a full-range timing scenario where all visible particles in the detector get assigned a time. In the long term, this approach to timing at ATLAS may become a reality. Due to the high rate of radiation exposure that the ITk will face in the HL-LHC, it will need to undergo regular replacements. This offers the opportunity for fairly frequent updates, including potential timing functionalities. If the HGTD proves successful, the technologies currently being developed for it could potentially be applied to 4D-tracking as well.[24]

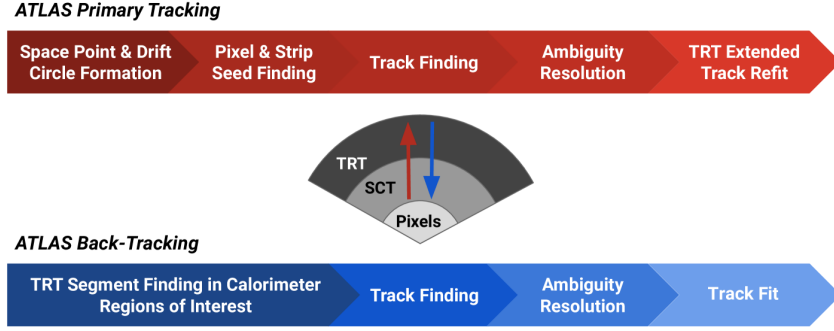


Figure 48: A simplified overview of ID track reconstruction methods.[8]

9 Appendix

9.1 Code

The results of this thesis were produced using the `HGTD_Analysis` package, available in Athena releases 24+. This package was developed to study performance of HGTD simulation. Within `HGTD_Analysis` the `HGTDTrackTimeInterface`[23] package is used to compute track-time. For the track-time association studies in this thesis, the `HGTD_PerformanceNtuple` algorithm was developed. For the isolation studies Athena’s `TrackIsolationTool` was used together with the `HGTD_MuonTrackStudies` algorithm developed for this thesis.

9.2 Track Reconstruction

Track reconstruction starts by clustering signals from adjacent channels in the silicon detectors into deposits likely originating from the same passing particle. These clusters are transformed into three-dimensional spatial hits, *space points* (*SP*), that can be used for track reconstruction. ATLAS uses two main strategies for track reconstruction; inside-out or outside-in. Figure 48 shows an overview of these methods. The primary tracking approach starts by matching sets of three space points that could have originated from the same particle. These sets are then used as seeds for track extrapolation.[8]

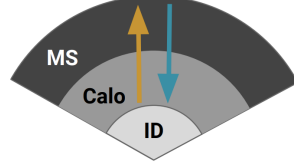
Search roads are constructed by matching track seeds to detector modules likely to contain compatible hits along an estimated seed trajectory. Fitting for a full track trajectory over a subset of detector modules instead of all possible hits greatly reduces computational time. The track seeds are extrapolated along these search roads with a combinatorial Kalman filter, which attempts to extend tracks both ways in r while smoothing them out. The resulting set of track candidates spanning the Pixel and SCT layers of the ID, still contains ambiguities in need of resolution, due to the relative imprecision of the Kalman filter method. Ambiguity resolution solves overlapping tracks and filters out incorrectly assigned clusters. The remaining track candidates are refit using a global χ^2 method to produce high precision estimates of the track parameters. In the $|\eta| < 2.0$ range, an attempt is made to extend these tracks to the TRT sub-detector. Similarly to the Pixel and SCT track finding procedure, the track candidates are used as seeds to form search roads in the TRT volume. Compatible TRT hits are then added to the existing tracks and a new global χ^2 fit is applied to the full collection of hits. If the addition of TRT tracks reduces the overall fit quality, only the Pixel + SCT track is retained.[8]

9.3 Muon Reconstruction Continued

Muon reconstruction is primarily done using an outside-in matching procedure, starting at the muon spectrometer tracks and attempting to match them to ID traces. This procedure is supplemented with a secondary inside-out chain that starts with extending ID tracks through the calorimeter and matching them to MS tracks. Figure 49 illustrates these two approaches.

Around 95% of muon candidates are identified in the outside-in reco-chain. Outside-in reconstruction starts by matching straight-line track segments in the MS into a single curved trajectory. After numerous

ATLAS Muon Outside-In



ATLAS Muon Inside-Out



Figure 49: Schematic of muon reconstruction methods.[12]

fit-quality selections, these tracks are then extrapolated to the beam line and the fit is corrected for the calorimeter contribution. Outside-in reconstruction can yield three types of muons;

- *Combined Muons*: For MS tracks within $|\eta| < 2.5$ an attempt is made to match them to an ID track. This is done by collecting all angularly compatible ID tracks in the $\eta - \phi$ plane around the MS track. To each of these tracks a full fit of all ID and MS measurements is applied.
- *Silicon-Associated Forward Muons*: In the Run 3 Inner Detector, no full tracks are available in the $|\eta| > 2.5$ range. Rather, MS tracks in this range can only be matched to short Pixel track segments. These are called *silicon-associated forward*.
- *Stand-Alone Muons*: If no compatible ID track is found, a MS track can be extrapolated to the beam line and be classified as *stand-alone*.

In the case of inside-out reconstruction, ID tracks are extrapolated through the MS. These extrapolated tracks are defined by their predicted crossing points and momentum inside the MS chambers. In order to minimise resources needed for this computationally heavy step, only ID tracks that have not yet been used in a muon reconstruction are considered. These extrapolated ID track trajectories serve as the starting points for inside-out reconstruction algorithms.

- *Segment-Tagged Muons*: Muons with very low p_T tend to reach no further than the first MS layer. To reconstruct such muons, the extrapolated ID track seeds are matched to spatially and momentum compatible MS segments. If at least one fitting segment is found, the muon is categorised as *segment-tagged*. The MS segment is not used to refit the track, but rather only for particle identification.
- *Calorimeter-Tagged Muons*: *Calorimeter-tagged muons* are reconstructed without MS information. In the $|\eta| < 0.1$ range, there is a gap in the Muons Spectrometer to allow space for ID and calorimeter cabling. To compensate, an attempt is made to match tracks in this range to minimum ionising particle signatures within the calorimeter. If a sufficient match can be made, these tracks may be identified as muons.
- *Combined Muons*: After the outside-in reconstruction phase, another attempt is made to recover *combined muons* using an inside-out matching procedure. This mainly improves the reconstruction rate of low- p_T muons.

For the HL-LHC phase of the ATLAS detector, the MS will similarly be matched to ITk tracks for muon reconstruction.[12]

References

- [1] ATLAS Collaboration, “The ATLAS experiment at the CERN Large Hadron Collider: a description of the detector configuration for Run 3,” *Journal of Instrumentation*, vol. 19, no. 05, P05063, May 2024, ISSN: 1748-0221. DOI: 10.1088/1748-0221/19/05/P05063. arXiv: 2305.16623. [Online]. Available: <https://cds.cern.ch/record/2859916>.
- [2] “CERN-Brochure-2017-002-Eng,” 2017. [Online]. Available: <https://cds.cern.ch/record/2255762>.
- [3] ATLAS Collaboration, “Technical Design Report: A High-Granularity Timing Detector for the ATLAS Phase-II Upgrade,” CERN, Geneva, Tech. Rep., 2020. [Online]. Available: <https://cds.cern.ch/record/2719855>.
- [4] JabberWok, *A graphic showing the relationship between angle and pseudorapidity*. May 16, 2007. [Online]. Available: <https://commons.wikimedia.org/wiki/File:Pseudorapidity2.png> (visited on 11/25/2024).
- [5] J. Pequenaio, “Computer generated image of the whole ATLAS detector,” 2008. [Online]. Available: <https://cds.cern.ch/record/1095924>.
- [6] S. Mehlhase, “ATLAS detector slice (and particle visualisations),” 2021. [Online]. Available: <https://cds.cern.ch/record/2770815>.
- [7] O. Brüning and L. Rossi, “The High-Luminosity Large Hadron Collider,” *Nature Reviews Physics*, vol. 1, no. 4, pp. 241–243, Apr. 2019, ISSN: 2522-5820. DOI: 10.1038/s42254-019-0050-6. [Online]. Available: <https://www.nature.com/articles/s42254-019-0050-6> (visited on 09/02/2024).
- [8] “ATLAS Track Reconstruction – General Overview,” ATLAS Software Documentation. (), [Online]. Available: <https://atlassoftwaredocs.web.cern.ch/internal-links/tracking-tutorial/idoverview/> (visited on 09/03/2024).
- [9] A. T. L. A. S. Collaboration. “Expected Tracking Performance of the ATLAS Inner Tracker at the High-Luminosity LHC.” arXiv: 2412.15090 [hep-ex]. (Dec. 19, 2024), [Online]. Available: <http://arxiv.org/abs/2412.15090> (visited on 12/25/2024), pre-published.
- [10] “Computational Performance of the ATLAS ITk GNN Track Reconstruction Pipeline,” CERN, Geneva, Tech. Rep., 2024. [Online]. Available: <https://cds.cern.ch/record/2914282>.
- [11] ATLAS Collaboration, “Development of ATLAS Primary Vertex Reconstruction for LHC Run 3,” 2019. [Online]. Available: <https://cds.cern.ch/record/2670380> (visited on 11/19/2024).
- [12] ATLAS Collaboration, “Software Performance of the ATLAS Track Reconstruction for LHC Run 3,” *Computing and Software for Big Science*, vol. 8, no. 1, p. 9, Dec. 2024, ISSN: 2510-2036, 2510-2044. DOI: 10.1007/s41781-023-00111-y.
- [13] S. Rettie, “Muon identification and performance in the ATLAS experiment,”
- [14] “Muon Selection Tool :” ATLAS Muon Combined Performance. (), [Online]. Available: <https://atlas-mcp.docs.cern.ch/guidelines/muonselectiontool/index.html> (visited on 11/28/2024).
- [15] “Athena basics,” ATLAS Software Documentation. (), [Online]. Available: <https://atlassoftwaredocs.web.cern.ch/athena/basics/> (visited on 11/19/2024).
- [16] “ATLAS Open Data Documentation | ATLAS Open Data.” (), [Online]. Available: https://opendata.atlas.cern/docs/documentation/introduction/introductory_page (visited on 11/20/2024).
- [17] “Geant4 Documentation,” Geant4. (), [Online]. Available: <https://geant4.web.cern.ch/docs/> (visited on 12/27/2024).
- [18] “Isolation Variables :” ATLAS Isolation and Fake Forum. (), [Online]. Available: <https://atlas-iff.docs.cern.ch/isolationvars/index.html> (visited on 11/28/2024).
- [19] “ATLAS Muon Combined Performance Working Group :” ATLAS Muon Combined Performance. (), [Online]. Available: <https://atlas-mcp.docs.cern.ch/index.html> (visited on 12/16/2024).
- [20] ATLAS Collaboration, “Expected tracking and related performance with the updated ATLAS Inner Tracker layout at the High-Luminosity LHC,” CERN, Geneva, Tech. Rep., 2021. [Online]. Available: <https://cds.cern.ch/record/2776651>.

- [21] A. D. Gentry and L. Pascual Dominguez, “Forward Electron Tracking Isolation for HL-LHC,” 2023. [Online]. Available: <https://cds.cern.ch/record/2852536>.
- [22] “Reconstruction/RecoTools/IsolationTool/Root/TrackIsolationTool.cxx · main · atlas / athena · GitLab,” GitLab. (Oct. 2, 2023), [Online]. Available: <https://gitlab.cern.ch/atlas/athena/-/blob/main/Reconstruction/RecoTools/IsolationTool/Root/TrackIsolationTool.cxx> (visited on 11/28/2024).
- [23] “Atlas-hgtd / SimulationAndPerformance / HGTDTrackTimeInterface · GitLab,” GitLab. (May 13, 2024), [Online]. Available: <https://gitlab.cern.ch:8443/atlas-hgtd/SimulationAndPerformance/HGTDTrackTimeInterface> (visited on 12/25/2024).
- [24] “Investigating the impact of 4D Tracking in ATLAS Beyond Run 4,” CERN, Geneva, Tech. Rep., 2023. [Online]. Available: <https://cds.cern.ch/record/2870326>.